The effects of dynamical degrees of freedom on magnetic compass sensitivity: A comparison of plant and avian cryptochromes

Gesa Grüning,[*,†] Siu Ying Wong,[†] Luca Gerhards,[†] Fabian Schuhmann,[†] Daniel R. Kattnig,[‡] P. J. Hore,[¶] and Ilia A. Solov'yov[*,†,§,‖]

†*Department of Physics, Carl von Ossietzky University, Carl-von-Ossietzky-Str. 9-11, 26129 Oldenburg, Germany*

‡*Department of Physics and Living Systems Institute, University of Exeter, Stocker Road, Exeter, EX4 4QD, United Kingdom*

¶*Department of Chemistry, University of Oxford, Physical and Theoretical Chemistry Laboratory, Oxford, OX1 3QZ, United Kingdom*

§*Research Center for Neurosensory Science, Carl von Ossietzky Universität Oldenburg, 26111 Oldenburg, Germany*

‖*Center for Nanoscale Dynamics (CENAD), Carl von Ossietzky Universität Oldenburg, Institut für Physik, Ammerländer Heerstr. 114-118, 26129 Oldenburg, Germany*

E-mail: gesa.gruening@uni-oldenburg.de; ilia.solovyov@uni-oldenburg.de

Abstract

The magnetic compass of migratory birds is thought to rely on a radical pair reaction inside the blue-light photoreceptor protein cryptochrome. The sensitivity of such a sensor to weak external magnetic fields is determined by a variety of magnetic interactions, including electron-nuclear hyperfine interactions. Here, we investigate the implications of thermal motion, focussing on fluctuations in the dihedral and librational angles of flavin adenine dinucleotide (FAD) and tryptophan (Trp) radicals in cryptochrome 4a from European robin (*Erithacus rubecula*, ErCry4a) and pigeon (*Columba livia*, ClCry4a) and cryptochrome 1 from the plant *Arabidopsis thaliana* (AtCry1). Molecular dynamics simulations and density functional theory-derived hyperfine interactions are used to calculate the quantum yield of radical pair recombination dependent on the direction of the geomagnetic field. This quantity and various dynamical parameters, are compared for [$FAD^{\bullet-}$ $Trp^{\bullet+}$] in ErCry4a, ClCry4a and AtCry1 with TrpC or TrpD the third and fourth components of the tryptophan triad/tetrad in the respective proteins. We find that (i) differences in the average dihedral angles in the RPs are small, (ii) the librational motions of $TrpC^{\bullet+}$ in the avian cryptochromes are appreciably smaller than in AtCry1, (iii) the rapid vibrational motions of the radicals leading to strong fluctuations in the hyperfine couplings affect the spin dynamics depending on the usage of instantaneous or time-averaged interactions. Future investigations of radical pair compass sensitivity should therefore not be based on single snapshots of the protein structure but should include the ensemble properties of the hyperfine interactions.

Introduction

The ability to detect the direction of the Earth's magnetic field occurs in a wide variety of animals.[1–5] The scale on which this poorly understood sense is exploited in Nature is impressively illustrated by the tens of billions of migratory birds that use the Earth's magnetic field each year to navigate to their wintering grounds and back.[6,7] The underlying biophysical mechanism is believed to involve macroscopic biological processes linked to microscopic quantum mechanical effects.[8] The latter seem to be essential to explain the influence of magnetic fields as weak as that of the Earth on animal behaviour.[2,8,9] The primary detection events are believed to occur in cryptochrome proteins in which a bound flavin adenine dinucleotide (FAD) cofactor and a chain of tryptophan (Trp) amino acid residues are key components in the activation of the protein and its response to external magnetic fields.[10] Blue-light excitation of the fully oxidised state of FAD triggers a cascade of electron transfers leading to the creation of a radical pair (RP) comprising $FAD^{\bullet-}$ and $Trp^{\bullet+}$. Creation of this state is typically rapid, occurring on a timescale of 30-220 ps in cryptochromes and homologous photolyases[11–15].

As shown in Fig. 1, RPs can exist in two limiting states, singlet and triplet, that differ only in their total electron-spin angular momentum. An external magnetic field, for example that of the Earth, can affect the extent and timing of coherent singlet-triplet interconversion and hence alter the yields of subsequent spin-selective reactions.[8,16,17] The change in the reaction yield is thought to form the basis of a biological sensor that could transduce information on the animal's heading.[16,18,19] While a detailed discussion of the signaling pathway[20,21] and the reaction products is beyond the scope of the present work, it is noted that [$FAD^{\bullet-}$ $Trp^{\bullet+}$] forms long-lived, stabilized states involving neutral tryptophan or tyrosine radicals *in vitro*.[19,22–24] As the longer lifetimes of such stabilized radical pairs render them unsuitable for magnetic sensing (any associated magnetic field effects would be destroyed by

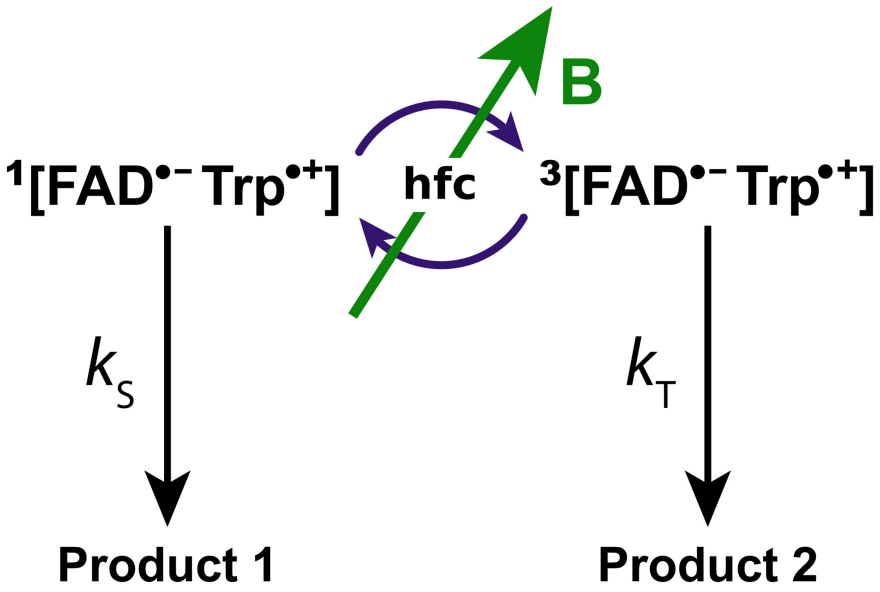

Figure 1: Simplified RP reaction scheme leading to magnetosensitive yields of reaction product states. [FAD$^{\bullet-}$ Trp$^{\bullet+}$] is the RP investigated here. The superscripts 1 and 3 indicate the singlet and triplet states. Different interactions drive the interconversion of singlet and triplet states; here only the hyperfine coupling (hfc) and the Zeeman interaction with the external magnetic field **B** are considered. The strength and direction of **B** influence the probability that the RPs are singlet or triplet. The RP can react to form the product states 1 or 2. We assume that the two rate constants, k_S and k_T are equal to 10^6 s^{-1}. In the spin dynamics calculations, the magnitude of **B** was 50 μT, typical of the geomagnetic field at intermediate latitudes.

spin relaxation), it is sufficient to focus on [FAD$^{\bullet-}$ Trp$^{\bullet+}$] exclusively.

Proof-of-principle experiments on model RP systems suggested that this mechanism might indeed explain the biological perception of weak magnetic fields.[23,25] Furthermore, RPs are known to be formed *in vitro* in proteins of the cryptochrome/photolyase family in non-migratory organisms.[19,26] Recent experiments demonstrated that the photochemistry and magnetic sensitivity of cryptochrome 4a from a migratory bird, the European robin (*Erithacus rubecula*, ErCry4a), appear to be suitable for magnetoreception.[25] Such findings support the hypothesis that the RP mechanism underlies compass magnetoreception in migratory animals. Efficient functioning of a RP-based compass in migratory birds requires

the RP to persist in a coherent spin state long enough for the Earth's magnetic field to have a significant influence on the spin dynamics. This mandates that loss of coherence (i.e. spin relaxation) arising from internal motions of the protein is sufficiently slow.[27] Note that, effects of internal protein motions on quantum states are also instrumental in the operation of other biological mechanisms such as light-harvesting in photosynthesis.[28–31]

ErCry4a appears to be more sensitive to magnetic fields than related cryptochromes from non-migratory species[25] but the origin of this difference is unknown. We have therefore compared ErCry4a with the much better characterized cryptochrome 1 from the plant *Arabidopsis thaliana* (AtCry1). A number of differences between ErCry4a and AtCry1 can be anticipated. For example, variations in protein dynamics can affect the rates of spin relaxation. More obviously, the two proteins differ in the number of Trp residues used to reduce the photo-excited FAD: three in AtCry1 and four in ErCry4a. In both cases, the terminal tryptophan, furthest from the FAD, acts as the ultimate electron donor.[25,32] RPs containing the third and fourth tryptophan radicals ($TrpC^{\bullet+}$ and $TrpD^{\bullet+}$) are denoted RPC and RPD.[25,33] It is not yet clear whether RPC, RPD, or both, are responsible for the magnetic sensitivity of ErCry4a[34]; in AtCry1 the magnetosensitivity originates from RPC.

In particular, we focus here on the RPC and RPD states of ErCry4a and the RPC state of AtCry1 (henceforth denoted ErC, ErD and AtC, respectively) in order to understand more clearly the connection between compass sensitivity and intramolecular motions. The RPC and RPD states (ClC and ClD) of pigeon (*Columba livia*) cryptochrome 4a (ClCry4a), from which a structure of ErCry4a was constructed via homology modelling,[25,35] were also studied and compared with the results for AtCry1 and ErCry4a. It was found in an earlier study that the dynamical behaviour of ErCry4a and ClCry4a differ even though ErCry4a was constructed using ClCry4a as a homology template.[35,36] Molecular dynamics (MD) simulations provide a valuable tool to investigate the dynamics of biomolecules,[37,38] including local dynamical fluctuations of small molecules bound to proteins.[39–42] Here, MD simula-

tions were performed to determine relevant structural and dynamic properties of $Trp^{\bullet+}$ and $FAD^{\bullet-}$ in the five RP states from which the most important hyperfine interactions were calculated using density functional theory (DFT). Finally, the magnetic sensitivity of AtCry1 and ErCry4a were compared using the time-averaged hyperfine interactions to simulate the quantum yields of the reaction products by means of the spin dynamics software package MolSpin.[43]

Methods

We have investigated the influence of specific motions on the magnetic sensitivity of AtCry1, ErCry4a and ClCry4a. For this purpose, three types of calculations were carried out: MD simulations of the cryptochrome structures, electronic structure calculations of the hyperfine couplings in $FAD^{\bullet-}$ and $Trp^{\bullet+}$ and spin dynamics simulations to determine the quantum yields of the RP reactions.

Molecular dynamics simulations

There being no crystal structure of ErCry4a, we have used a homology model developed in a previous study[25,35,36] by matching the amino acid sequence of ErCry4a[32] to the known crystal structure of ClCry4a (PDB ID: 6PU0).[44] All-atom MD simulations were performed for the RPC and RPD states of ErCry4a using NAMD,[45,46] employing the VIKING online-platform[47] to set up the calculation. Simulations of ErCry4a solvated in an aqueous solution of 50 mM NaCl contained $100,518$ atoms and were run for 400 ns. Three replica simulations were performed for each RP state of ErCry4a to improve the statistical significance. Thus, three simulations contained the oxidised $TrpC^{\bullet+}$ residue (W318) and three contained $TrpD^{\bullet+}$ (W369) as the partner of the flavin radical, $FAD^{\bullet-}$. As a starting point, the simulations used radical charges and structures from a previous study of ErCry4a,[25] which, having been run

for more than 200 ns, were considered well-equilibrated. A similar approach was used for ClCry4a again using trajectories from a previous study[48] as a starting point. In this case, the solvated system, including 50 mM NaCl, resulted in 121,097 atoms. Three replica simulations were carried out for 400 ns each. For AtCry1, the MD trajectories from an earlier study[27] were extended to obtain three replica 400 ns simulations for the AtC state. The CHARMM36 force-field with CMAP corrections was used to model standard residues in the protein,[49–51] the TIP3P model was used for the water,[49,52] and the temperature was maintained at 310 K with a Langevin thermostat. In the studies of the librational motions of the radicals, the protein structures in each simulation were aligned using VMD[53] by minimising the difference in the positions of all backbone Cα atoms in each MD frame from the corresponding Cα positions in the first frame of the production simulation. The alignment procedure does not unnaturally restrict or distort variations in the librational angles of $FAD^{\bullet-}$ and $Trp^{\bullet+}$ since the angles are defined using the aromatic rings of the radicals, which do not contain Cα atoms.

Calculation of the hyperfine tensors

To calculate specific time-dependent properties of the radicals, $FAD^{\bullet-}$ and $Trp^{\bullet+}$ were excised from the MD trajectories and the dangling bonds terminated with hydrogen atoms.[27] The resulting structures, with 22 atoms in $Trp^{\bullet+}$ (truncated at the Cα-backbone bonds) and 47 in $FAD^{\bullet-}$ (truncated at the ribityl chain), are depicted in Fig. 2. All quantum chemical properties of the radicals were calculated using the program package Gaussian09.[54] The hybrid functional B3LYP and the 6-311G(d) basis set[55–57] were employed for the geometry optimisations of the terminal hydrogen atoms (Fig. 2, black circles). The positions of all other nuclei in the radicals were directly taken over from the MD simulations so that fluctuations in the hyperfine interactions due to the thermal motion could be sampled.

The resulting radical geometries were used to compute the hyperfine coupling tensors

using the purpose-built EPR-II basis set.[58] 1,000 DFT calculations were performed for both radicals in each of the five states. The 1,000 geometries were obtained by concatenating the three 400-ns replica simulations to produce a 1,200 ns trajectory from which geometries were extracted every 1.2 ns. DFT calculations for each radical gave the mean and variance of the hyperfine tensors for each magnetic nucleus. Subsequently, the hyperfine interactions were compared for (a) single configurations and (b) an average over 1,200 ns. For (a), the first three frames of a MD simulation, spaced 500 fs apart, were investigated. In addition, for AtCry1, we have considered the static geometry obtained from the crystal structure (PDB ID: 1U3C,[59] see Supplementary Material, Fig. S16).

Spin dynamics

Spin dynamics calculations employed the open-source program MolSpin[43] interfaced through the online-platform VIKING.[47] The program was used to calculate the quantum yield of the product formed from the singlet RP subject to an external magnetic field. This quantity is defined as:

$$\Phi_{\mathrm{S}} = k_{\mathrm{S}} \int_0^\infty \mathrm{Tr}(\hat{\mathrm{P}}_{\mathrm{S}} \hat{\rho}(\mathbf{B}, t)) dt. \tag{1}$$

Here, $\hat{\mathrm{P}}_{\mathrm{S}}$ is the projection operator onto the singlet state, Tr denotes trace, and the time-dependence of the density operator $\hat{\rho}(\mathbf{B}, t)$ is given by the stochastic Liouville equation (Supplementary Material). In this study only the hyperfine and Zeeman interactions were included in the spin Hamiltonian, the former calculated as described above. k_{S} is the singlet reaction rate constant and was assumed to be equal to the triplet reaction rate constant, k_{T} (see Fig. 1). The singlet yield averaged over all directions of the magnetic field vector $\mathbf{B}(\phi, \theta)$ is given by:

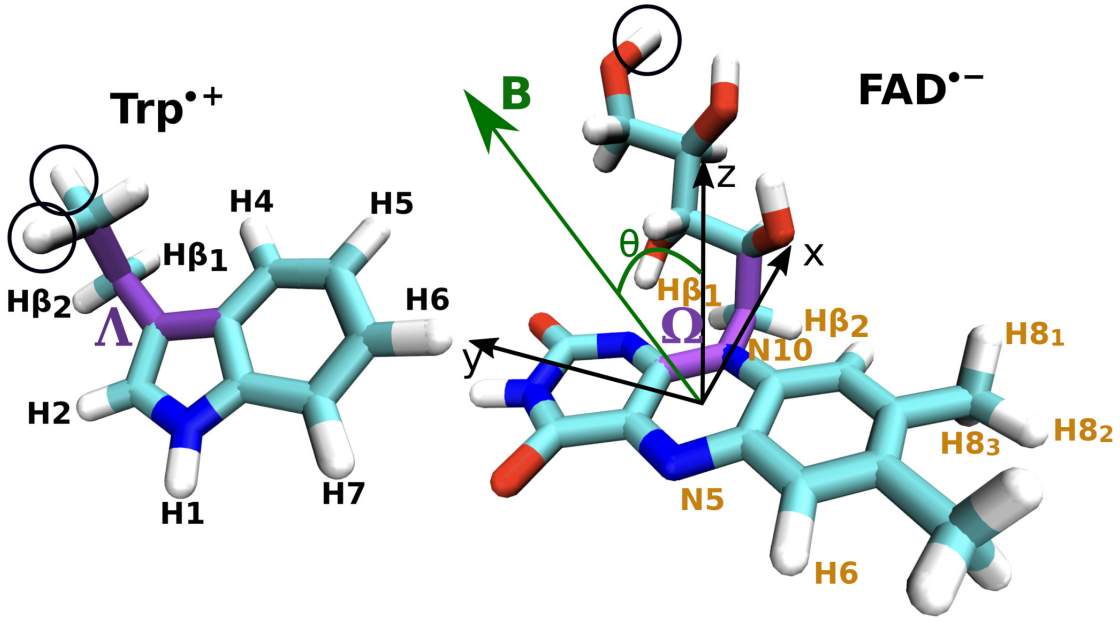

Figure 2: The $Trp^{\bullet+}$ and $FAD^{\bullet-}$ radicals from ErCry4a are shown with the terminal hydrogen atoms (circled) that were used to terminate the dangling bonds in the quantum calculations. Nuclei labelled in black and orange were included in the spin dynamics calculations by virtue of their significant average hyperfine couplings as obtained from DFT calculations. The dihedral angles Λ, spanned by Cα-Cβ-Cγ-Cδ2 in $Trp^{\bullet+}$, and Ω, spanned by C2′-C1′-N10-C10 in $FAD^{\bullet-}$, marked in purple, were found to be important in a previous study of spin relaxation in AtCry1.[27] The orientation of the magnetic field vector $\mathbf{B}$ is specified by θ, the angle between $\mathbf{B}$ and the z-axis of the isoalloxazine portion of $FAD^{\bullet-}$, and the azimuthal angle ϕ (not shown). The detailed definition of the molecular axes shown in black is given in Fig. S1.

$$\bar{\Phi}_{\mathrm{S}} = \frac{1}{2\pi}\int_0^{2\pi} d\phi \int_0^{\frac{\pi}{2}} d\theta \, \sin(\theta)\Phi_{\mathrm{S}}(\phi,\theta,\mathrm{B}_0). \tag{2}$$

The angles θ and ϕ, which define the orientation of the magnetic field (Fig. 2) were varied in steps of 5° in order to evaluate the integrals. The average singlet yield $\overline{\Phi}_{\mathrm{S}}$, together with the maximum and minimum values, $\Phi_{\mathrm{S,max}}$ and $\Phi_{\mathrm{S,min}}$ were used to obtain the singlet yield anisotropy Γ,

$$\Gamma = (\Phi_{\mathrm{S,max}} - \Phi_{\mathrm{S,min}})/(\bar{\Phi}_{\mathrm{S}}), \tag{3}$$

which is considered to be a measure of the magnetic compass sensitivity.[27] With this definition, a sensitive RP compass is characterised by a large variation in the reaction yield (large Γ) on changing the magnetic field direction.

The rate constant k_{S} was assumed to be 10^6 s^{-1} to give a RP lifetime of 1 μs, which allows enough time for an Earth-strength magnetic field ($|\mathbf{B}| = 50$ μT) to affect the spin dynamics[60] (see Supplementary Material, Fig. S20 for Γ values computed for reaction rate constants other than 10^6 s^{-1}). Electron exchange and dipolar couplings were omitted to make calculations of large spin systems computationally feasible and to allow for better comparability with earlier studies.[7,27,61] For the spin dynamics calculations, hyperfine coupling tensors for each of the nuclei labelled in Fig. 2 were averaged over 1,000 geometries as described above. The results of these simulations were compared with singlet yield anisotropies obtained for single MD frame geometries or the AtCry1 crystal structure.

Results and Discussion

Characterization of motion

The most relevant motions when considering the magnetic sensitivity of RPs in cryptochrome are those that cause significant fluctuations in the Zeeman and/or hyperfine interactions, i.e. the interactions of the electron spins with the external magnetic field and with the spins of magnetic nuclei, respectively. For this reason, a previous study (of AtCry1) focussed on the variations in the dihedral angles Λ and Ω shown in Fig. 2 and the librational (i.e. rocking) motions of the aromatic groups of $FAD^{\bullet-}$ and $Trp^{\bullet+}$ in the protein.[27] We have therefore

studied the same motions and parameters in ErCry4a and ClCry4a for comparison with AtCry1. To do so, probability distribution functions were calculated for these degrees of freedom.

Librational angles

The rocking motions of the aromatic groups of $FAD^{\bullet-}$ and $Trp^{\bullet+}$ can be parameterised by means of rotation angles around three orthogonal molecular axes and visualised as scatter plots (described in the Supplementary Material) on a spherical surface (Figs. 3A and 3B). From the spread of points within these plots, it is clear that both radicals in AtCry1 undergo more extensive librations than they do in ErCry4a and ClCry4a. Fits of the distributions of librational angles in AtC, ClC, ErC, ClD and ErD to a Rayleigh distribution (Figs. 3C-D) offer more quantitative insight into the dynamics. Although $FAD^{\bullet-}$ in AtC undergoes slightly larger amplitude librations for the x- and y-axes than the four avian RPs, there is little difference between the five environments (Fig. 3C). By contrast, $Trp^{\bullet+}$ is significantly less mobile (narrower distributions) in both ErCry4a RPs than it is in AtCry1 (Fig. 3D). ClC and ClD show distributions similar to those of the corresponding ErCry4a states, in good agreement with the visualizations in Fig. 3A and 3B.

The more pronounced motion of $Trp^{\bullet+}$ in AtC compared to the avian RP states can also be seen from the modes of the distributions of the librational angles (Table 1), with the values for AtC being about 3 degrees larger than for the other RP states. Additionally, it can be seen that $Trp^{\bullet+}$ in ErD has the smallest mode values for all three molecular axes.

Dihedral angles

The dihedral angles Ω and Λ shown in Fig. 2 were considered earlier[27] to be the degrees of freedom that would have the largest effect on the hyperfine couplings in $FAD^{\bullet-}$ and $Trp^{\bullet+}$, and would therefore constitute one of the main spin-relaxation channels resulting

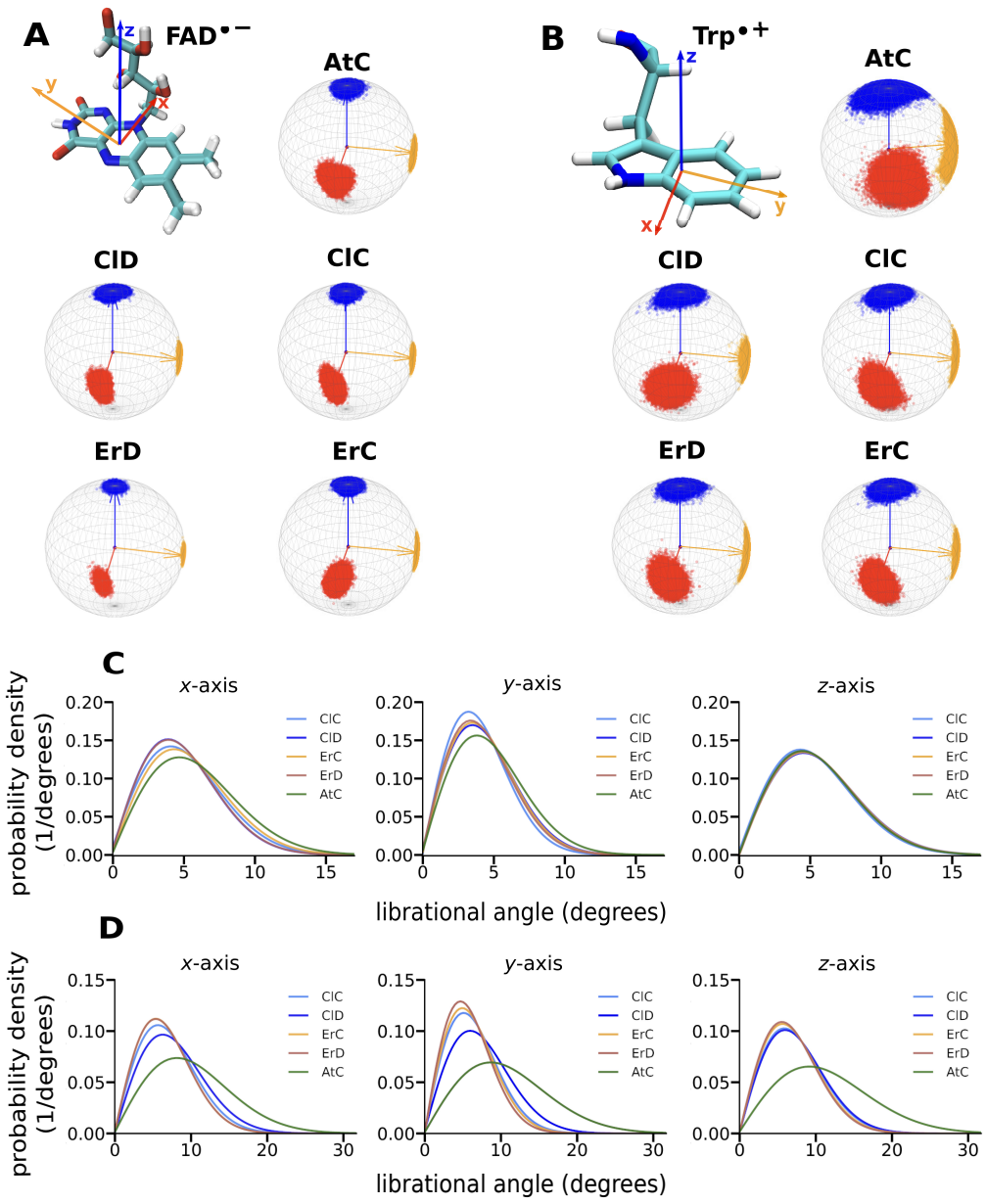

Figure 3: Spherical scatter plots for the librations of $FAD^{\bullet-}$ (**A**) and $Trp^{\bullet+}$ (**B**) showing the spread of directions of the molecular axes. For each RP system, 80,000 orientations are shown, selected at equal intervals from one 400-ns MD trajectory. **C** and **D**: fits of the librational angles in $FAD^{\bullet-}$ (**C**) and $Trp^{\bullet+}$ (**D**) to the Rayleigh distribution. The distributions (Figs S5, S6, S7, S8, S9, S10) are based on 80,000 values extracted from a 400-ns MD simulation. Each colour corresponds to a RP system and each column represents the librations around a different molecular axis.

Table 1: Modes of the Rayleigh distributions of the librational angles (in degrees) for $FAD^{\bullet-}$ and $Trp^{\bullet+}$ obtained from a 400-ns MD simulation for each RP state.

	RP	x-axis	y-axis	z-axis
$FAD^{\bullet-}$	AtC	4.7	3.9	4.5
	ClC	4.3	3.2	4.4
	ErC	4.4	3.5	4.5
	ClD	4.0	3.6	4.5
	ErD	4.0	3.4	4.5
$Trp^{\bullet+}$	AtC	8.2	8.7	9.3
	ClC	5.7	5.2	5.9
	ErC	5.4	5.0	5.7
	ClD	6.3	6.1	6.0
	ErD	5.4	4.7	5.6

from random thermal motion. Figure 4 and Table 2 compare these motions of $FAD^{\bullet-}$ and $Trp^{\bullet+}$. A broader probability density distribution (larger standard deviation) indicates a greater degree of motional freedom. The mean value of the Λ-distribution of ClC is smaller than that of AtC and ErC. Moreover, the Λ-distribution of ErC is narrower than those of AtC and ClC. The Λ-distributions of the RPD states are similar. The Ω-distributions of all the five RP states are similar.

To determine whether small differences in the distributions of dihedral angles could have a significant effect on the average hyperfine couplings, and therefore the magnetic sensitivity, DFT calculations were performed to obtain the dependence of the hyperfine coupling parameters on the two dihedral angles. Guided by the values observed in the MD simulations, Ω in $FAD^{\bullet-}$ was varied between 80° and 120° in steps of 2.5°, while Λ in $Trp^{\bullet+}$ ranged over -140° to -40° and 45° to 110° in steps of 5°. All other atomic coordinates, which were not connected to the dihedral angles, were not changed in the DFT calculations.

Analysis of the DFT calculations revealed that for the majority of the magnetic nuclei, there is little dependence of the hyperfine parameters on the dihedral angles: only Hβ_1 and Hβ_2 in $FAD^{\bullet-}$ and Hβ_1 and Hβ_2 in $Trp^{\bullet+}$ varied significantly with Ω and Λ respectively

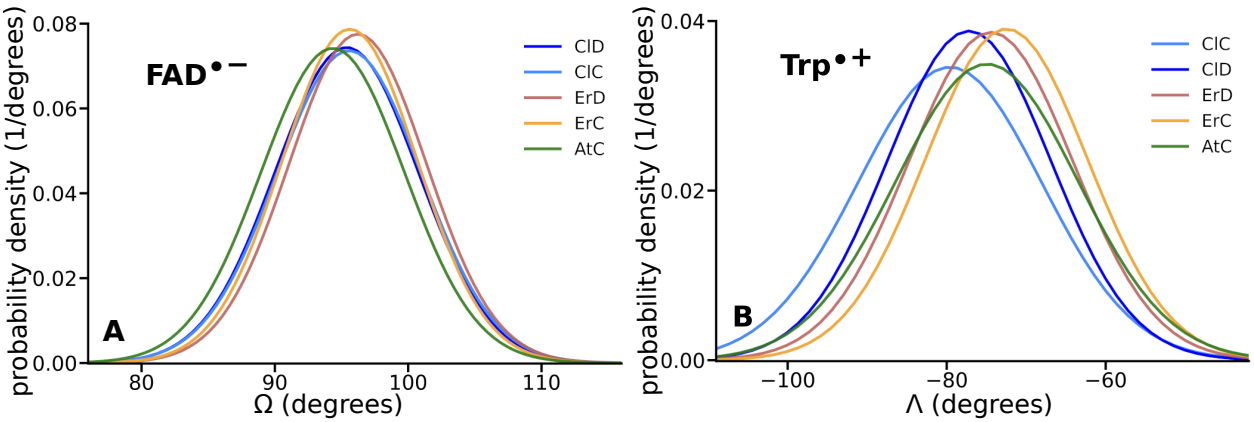

Figure 4: Gaussian fits to the distributions of the dihedral angles Ω in $FAD^{\bullet-}$ (**A**) and Λ in $Trp^{\bullet+}$ (**B**) determined from three replica MD simulations for each RP system. The Λ-distributions of ClD and ErD in **B** have been shifted by −150° to allow a better comparison with the RPC states.

(Fig. 5). Similar behaviour was found in a previous study (Supplementary Material of Ref.[27]) for AtCry1. The dihedral angles influence the efficiency of hyperconjugation between the aromatic ring and the Cβ-Hβ bonds and therefore the distributions of spin density at the two Hβ protons[62–64] in each radical, while the spin density at the magnetic nuclei in the aromatic rings is largely unaffected. Figure 5 also shows that the Hβ protons have much larger hyperfine interactions in $Trp^{\bullet+}$ than in $FAD^{\bullet-}$ suggesting that the dihedral angle Λ in $Trp^{\bullet+}$ may have a larger effect on the magnetic sensitivity than does Ω in $FAD^{\bullet-}$.

Having determined (i) the dependence of the $Trp^{\bullet+}$ Hβ_1 and Hβ_2 hyperfine couplings on Λ (Fig. 5) and (ii) the distributions of Λ in the MD simulations (Fig. 4), we can predict the distribution of the Hβ isotropic hyperfine coupling constants of $Trp^{\bullet+}$ in each RP state. Assuming that the interaction of the Hβ protons with the electron spin in $Trp^{\bullet+}$ is dominated by the hyperconjugation mechanism, the Λ-dependence of the isotropic coupling constants can be modelled using the Heller-McConnell equation[62–64] as

Table 2: Means and standard deviations (s.d.) (in degrees) of the Gaussian distributions of the dihedral angles Ω in $FAD^{\bullet-}$ and Λ in $Trp^{\bullet+}$ obtained from three replica MD simulations for each RP state.

angle	RP	mean	s.d.
Ω	AtC	94.3	5.4
	ClC	95.6	5.4
	ErC	95.6	5.1
	ClD	95.4	5.4
	ErD	96.2	5.2
Λ	AtC	-75.3	11.2
	ClC	-79.6	11.5
	ErC	-73.1	10.3
	ClD	72.8	10.3
	ErD	75.6	10.3

$$a_{\text{iso}} = A\cos^2(\Lambda - \Lambda_0) + a_0, \tag{4}$$

where the amplitude, A, and offset, a_0, are parameters. Λ_0 is the value of Λ at which the

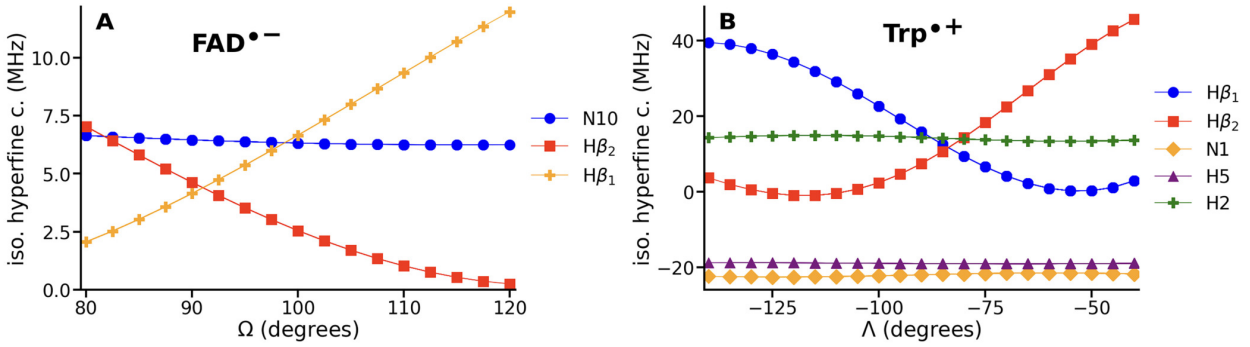

Figure 5: **A**: Dependence of the isotropic hyperfine coupling constants of selected nuclei in $FAD^{\bullet-}$ as a function of the dihedral angle Ω. Orange, red and blue indicate the values for Hβ_1, Hβ_2, and N10, respectively. **B**: A similar graph for Λ in $Trp^{\bullet+}$. Blue, red, orange, green and purple correspond to Hβ_1, Hβ_2, N1, H2 and H5 nuclei, respectively. In both radicals, the hyperfine couplings of the Hβ protons are strongly affected by a change in the dihedral angle, while the couplings for other nuclei remain largely unchanged.

Table 3: Means and standard deviations (in MHz) of the isotropic hyperfine couplings for the Hβ protons in $Trp^{\bullet+}$. The first five rows show values obtained from the distributions of the hyperfine couplings calculated for geometries extracted from the MD simulations. The last five rows give the expected couplings calculated from the Λ-distributions, as described in the text.

	RP system	$a_{iso}(H\beta_1)$	$a_{iso}(H\beta_2)$
MD	AtC	8.8 ± 8.7	30.8 ± 15.2
	ClC	10.7 ± 9.1	29.3 ± 14.5
	ErC	5.9 ± 6.2	37.0 ± 14.8
	ClD	37.4 ± 15.3	8.3 ± 7.4
	ErD	33.3 ± 14.0	10.1 ± 8.1
Λ	AtC	3.8 ± 3.9	22.4 ± 8.0
	ClC	6.1 ± 5.3	18.3 ± 8.3
	ErC	3.1 ± 3.2	23.5 ± 7.3
	ClD	23.3 ± 7.1	3.0 ± 3.3
	ErD	21.3 ± 7.3	4.0 ± 4.0

C-Hβ bond is rotated by 90° (around the Cβ-Cγ bond) out of the plane of the tryptophan ring. Fits of the data in Fig. 5B to Eq. (4) are shown in Fig. 6 and give the following parameters: $\Lambda_0 = 30°$, $A = 43$ MHz and $a_0 = 0.5$ MHz for Hβ1 and $\Lambda_0 = -28°$, $A = 45$ MHz and $a_0 = 0.2$ MHz for Hβ2. Figure 6 also shows the Gaussian distributions of the Λ angles obtained directly from the MD simulations for the five RPs as seen in Fig. 4. Averaging the fitted curves over the appropriate Λ-distribution gives the hyperfine couplings shown in the lower five rows of Table 3. The expected distributions of the Hβ_1 and Hβ_2 couplings are shown in Fig. S12. The distributions of isotropic Hβ coupling constants were also obtained from frame-by-frame DFT calculations for each MD trajectory (Fig. S11). The average values are given in the upper five rows of Table 3. Two points are apparent from Table 3. First, the hyperfine couplings estimated by the two methods are markedly different, especially for the larger of the two interactions in each RP (Hβ_2 in the RPC states, Hβ_1 in the RPD states). Clearly, the dihedral angle Λ is not the only factor affecting the Hβ hyperfine couplings. All of the hyperfine couplings have large standard deviations reflecting

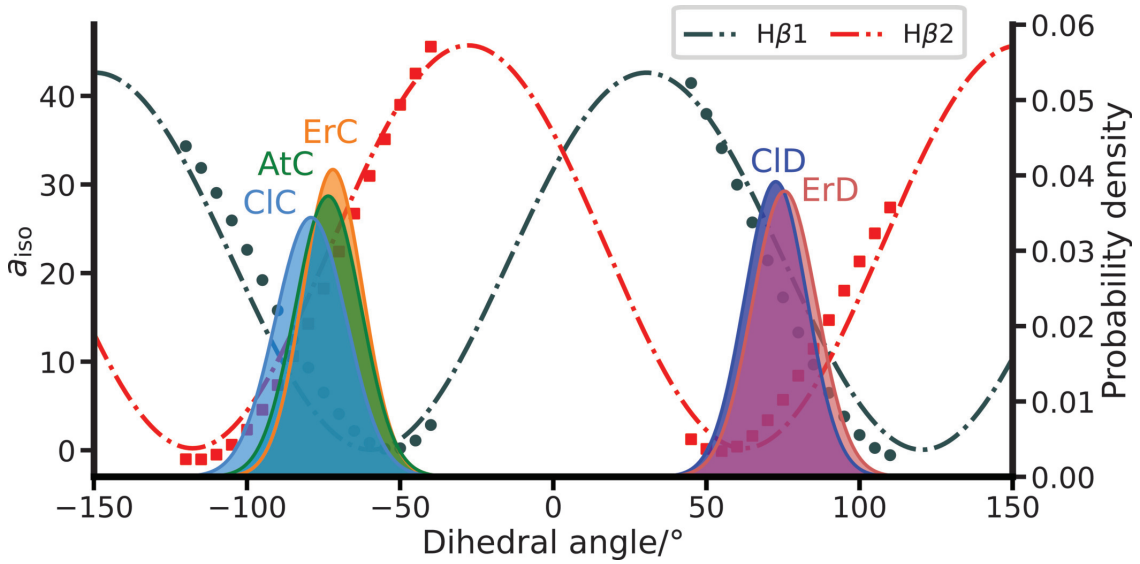

Figure 6: The distributions in green, light blue, orange, blue and red show the values of the dihedral angle Λ during the 1200 ns interval covered in the three replica MD simulations for AtC, ClC, ErC, ClD and ErD, respectively (right axis). The dark green dots and red squares show the values of the isotropic hyperfine coupling (left axis) from the DFT calculation where only Λ was changed and all other nuclei positions in the Trp remained fixed. The dark green and red lines are fits of the data to Eq. (4).

the broad distributions seen in Fig. 4 and Fig. 6. Second, the MD method gives larger variations between RPs. For example, the average value for Hβ_2 in AtC differs from that in ErC by 6.2 MHz in the MD case and by only 1.1 MHz for the Λ-method. Additionally, while the a_{iso} values for the two RPD states are similar, the values for ClC and ErC are notably different (Welch's t-test: $p < 0.05$ for both Hβ a_{iso} values), a noteworthy observation given that the ErCry4a structure was obtained via homology modelling from ClCry4a. In fact, the a_{iso} values of ClC are closer to the a_{iso} values of AtC than to ErC. We discuss below whether the differences in a_{iso} values are significant for the magnetic sensitivity of the RPs.

Average hyperfine coupling

To explore the influence of protein dynamics on the hyperfine interactions, we have compared the $\text{TrpC}^{\bullet+}$ hyperfine tensors averaged over a large number of MD frames with those for a

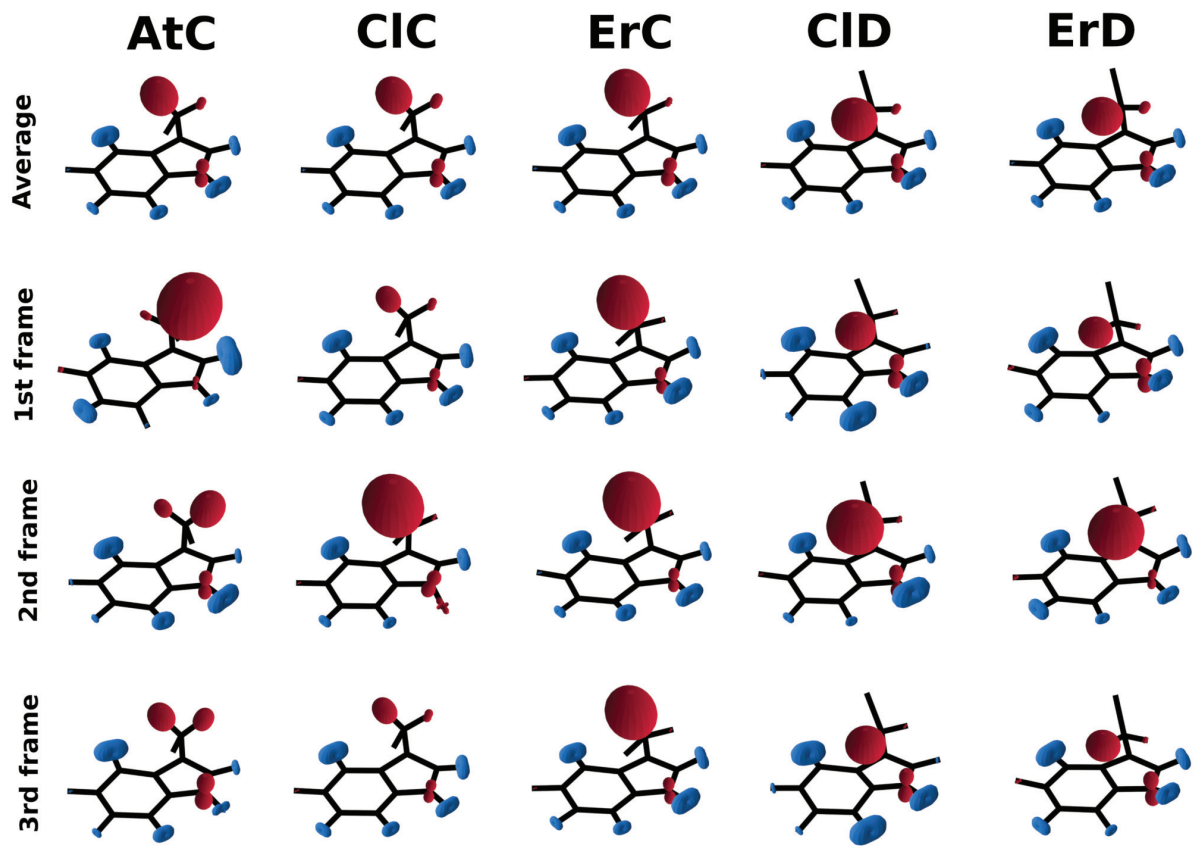

Figure 7: Three-dimensional surface plot representations of the full hyperfine tensors in $Trp^{\bullet+}$. Only interactions of the magnetic H- and N-nuclei are displayed. Red (blue) lobes indicate a positive (negative) value of the trace of the tensor with a larger lobe signifying a stronger hyperfine coupling and a more spherical lobe indicating a more isotropic hyperfine coupling tensor. Top row: average hyperfine tensors on black wireframes of the averaged coordinates, computed from 1,000 snapshots extracted from the three MD trajectories for each RP state, covering 1,200 ns of simulation time. Lower 3 rows: hyperfine tensors calculated from single MD frames, separated by 500 fs.

few individual frames (Fig. 7). To facilitate comparison, each of the 20 representations were rotated to the same orientation with the indole group in the xy-plane, i.e. librations are not visible in this figure. For the top row of the figure, the rotation was performed prior to averaging the hyperfine tensors. $Trp^{\bullet+}$ has similar average hyperfine interactions in all five RP states (Fig. 7, top row); the main differences are for the Hβ_1 and Hβ_2 nuclei reflecting

the different dihedral angles for ErD and ClD compared to ErC, ClC and AtC (Figs 5 and 6). In the RPC states, the hyperfine interaction of Hβ_2 is larger than that of Hβ_1, while the reverse is true for the RPD states. Among the three RPC states, ErC stands out with a larger ratio of the two Hβ couplings, which differentiates it from AtC and ClC. The hyperfine couplings in ErD and ClD however are similar.

The three lower rows in Fig. 7 illustrate the hyperfine interactions computed for static geometries taken as single frames from the MD simulations at intervals of 500 fs. There are clear variations on this fast time-scale, in particular for Hβ_1 and Hβ_2 but also for some of the indole protons. For $FAD^{\bullet-}$, by contrast (Fig. S17), there are smaller differences between the averaged and single-frame hyperfine tensors implying that single-geometry spin dynamics simulations are less likely to be unrepresentative than in the case of $Trp^{\bullet+}$. Furthermore, there are no large differences in the $FAD^{\bullet-}$ hyperfine tensors for the five RP states consistent with Figs 3A and 4A.

In conclusion, the hyperfine interactions for the $Trp^{\bullet+}$ radicals are more likely than those in $FAD^{\bullet-}$ to lead to differences in the average magnetic sensitivities of AtCry1, ErCry4a and ClCry4a.

Magnetic sensitivity

The differences in the average and single-geometry hyperfine interactions described in the previous section can be expected to affect the sensitivity of the five RP states to the direction of a weak external magnetic field. We have therefore calculated the singlet yield anisotropy Γ using Eq. (3) for AtC, ErC and ErD. We have chosen to perform calculations comparing AtC, ErC and ErD only because the two proteins come from two very different organisms. A comparison of ErC/ErD and ClC/ClD would also be possible but would require significant computational resources, which are difficult to justify given the similarity of ClC to AtC and ClD to ErD. Figures 8-10 show the anisotropic components of the reaction yield

$\Phi_S(\mathbf{B}(\theta,\phi))$ (referred to as anisotropy surface plots[34]). Other factors being equal, the larger the anisotropy surface and the greater the value of Γ, the more magnetically sensitive the RP should be.

Difference between single frame and average hyperfine interactions

Figure 8 shows anisotropy surface plots for the three RP states computed using hyperfine interactions averaged over the entire MD simulation and for three single MD frames. Substantial variations in the size and shape of the singlet yield anisotropy are evident for the three RP states and the four sets of hyperfine interactions. Similar differences were found for AtC using hyperfine tensors calculated from the crystal structure (Fig. S18). These results show that the magnetic sensitivity cannot reliably be established on the basis of a single static geometry of the RP, as has often been done in the past.[7,34,61,65] In the following, we rely exclusively on calculations using the average hyperfine couplings which should give a better idea of the magnetic sensitivity. Additionally, a stronger focus will be placed on different parameters and their influence on the general magnetic sensitivity.

Influence of Λ on the compass sensitivity

The main difference in the average hyperfine couplings of the three RP states (AtC, ErC and ErD) occurs for the Hβ nuclei of $Trp^{\bullet+}$ (Fig. 7) which are much more sensitive to the dihedral angle Λ than other nuclei (Fig. 5). However Λ is not the only factor that affects the Hβ couplings (Table 3) and only a small difference in the widths of the Λ-distributions for the different RP systems has been found (Fig. 4 and Table 2).

To determine how much these variations affect the magnetic sensitivity, the hyperfine coupling tensors of the Hβ nuclei have been altered in different ways (Fig. 9). The most direct approach is to exchange the average isotropic hyperfine couplings of the Hβ nuclei in $TrpC^{\bullet+}$ in ErC with those in $TrpC^{\bullet+}$ in AtC. As shown in the second row of Fig. 9, this

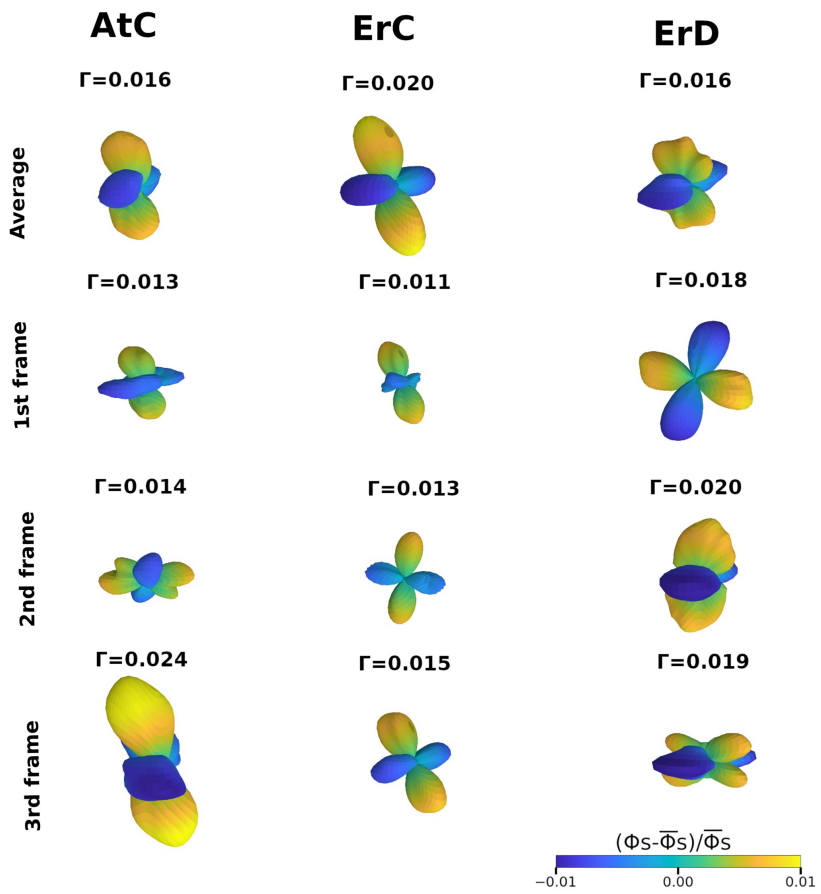

Figure 8: Anisotropy surface plots showing the relative anisotropic component of the singlet yield for spherically distributed directions of a 50 μT external magnetic field. The RPs in all calculations included the N5, N10, $H8_1$, $H8_2$ and $H8_3$ nuclei in $FAD^{\bullet-}$ and $H\beta_1$, $H\beta_2$, H1, N1 and H4 in $Trp^{\bullet+}$. The average of the hyperfine tensors was performed over 1200 ns of MD simulations. The geometries used to calculate the anisotropy surface plots in the lower three rows were taken from MD frames 500 fs apart.

affects the size of the anisotropy surface plots for both RP states, but not the overall shape. Nevertheless, swapping the hyperfine interactions reduces Γ from 0.016 to 0.013 for AtC and increases it from 0.020 to 0.023 for ErC, reflecting the different strengths of the isotropic $H\beta$ hyperfine couplings in AtC and ErC. ErC has a larger ratio of $H\beta_1$ to $H\beta_2$ hyperfine couplings than AtC which seems to reduce the anisotropy of the magnetic field effect. However, the average hyperfine couplings of the $H\beta$ nuclei in $Trp^{\bullet+}$ are influenced not only by Λ but also

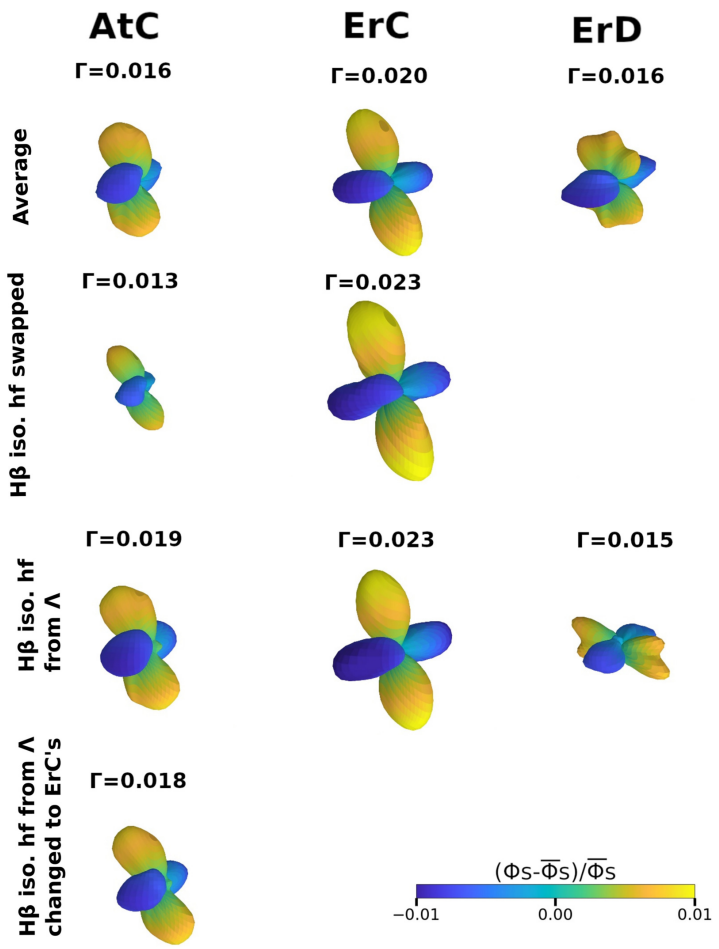

Figure 9: Anisotropy surface plots for AtC, ErC and ErD based on calculations containing N5, N10, $H8_1$, $H8_2$ and $H8_3$ in $FAD^{\bullet-}$ and $H\beta_1$, $H\beta_2$, H1, N1 and H4 in $Trp^{\bullet+}$. First row: calculations using the hyperfine interactions averaged over 1,200 ns of MD simulations. Second row: same as first row but with the averaged isotropic hyperfine couplings of the Hβ nuclei in AtC and ErC exchanged. Third row: same as first row but with the isotropic hyperfine interaction couplings of the Hβ nuclei changed to the value expected if the dihedral angle Λ were the sole determinant of their value (see Table 3). Fourth row: same as third row but with the isotropic Hβ hyperfine values for AtC changed to the isotropic Hβ hyperfine values predicted for ErC.

by other motions. To separate these two effects, we have replaced the isotropic components of the Hβ hyperfine coupling tensors in the RPs (upper three rows, Table 3) by the values obtained from the Λ-distributions using Eq. (4) (lower three rows, Table 3). The resulting

plots are shown in the third row of Fig. 9. As can be seen, the size but not the shape of the anisotropy plots for AtC and ErC changes, comparing rows 1 and 3 in the figure. Thus, for ErC and AtC, the effect of using the isotropic hyperfine coupling values from the bottom half of Table 3 instead of the top half is relatively small. Therefore we can conclude that, in this case, factors other than the dihedral angle are dominant. It is however striking that, for ErD significant changes in the shape of the singlet yield anisotropy plots can be observed while the corresponding Γ values remain similar.

Lastly, the question of whether the differences in the Λ-distributions of the RPs (Fig. 4) have a significant impact on the compass sensitivity still remains. To address this, the isotropic components of the Hβ couplings in AtC predicted from the Λ-distributions were replaced with the corresponding values for ErC. This substitution hardly affects the shape or the value of Γ (Fig. 9, fourth row). We can thus conclude that differences in the average dihedral angle Λ will not have a large influence on the compass sensitivity of the radical pairs.

Number of hyperfine interactions included

The RPs considered here contain a total of 27 hyperfine interactions: 15 in $FAD^{\bullet-}$ and 12 in $Trp^{\bullet+}$. As the inclusion of 27 hyperfine interactions is computationally too demanding for a systematic study, it is necessary to select which nuclei to include in the calculation. The results in previous sections, obtained using spin systems with ten nuclei, incorporated the most important hyperfine interactions in $FAD^{\bullet-}$ and $Trp^{\bullet+}$ while still being computationally feasible. In this section, spin systems are built up one nucleus at a time so as to gain insight from the trends in the magnetic sensitivity of the various RPs. By including the hyperfine interactions in descending order of importance, one could obtain a realistic picture of the trends in the asymptotic reaction yield anisotropy of [$FAD^{\bullet-}$ $Trp^{\bullet+}$] without the calculations being excessively time-consuming.

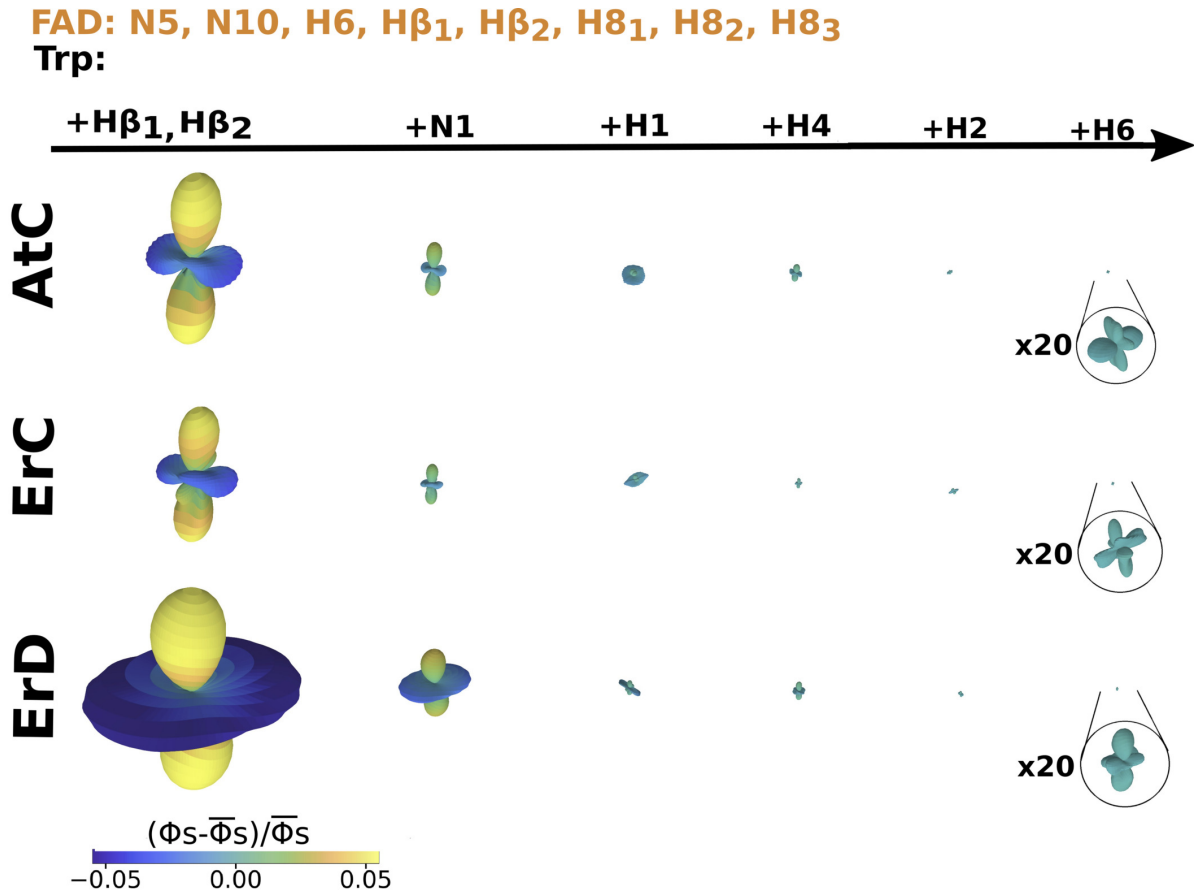

Figure 10: Anisotropy surface plots for RPs with different numbers of hyperfine couplings. The top, middle and bottom rows show results for AtC, ErC and ErD, respectively. The first plot in each row shows the singlet yield anisotropy for a RP containing N5, N10, Hβ_1, Hβ_2, H6, H8_1, H8_2 and H8_3 in $FAD^{\bullet-}$ and Hβ_1 and Hβ_2 in $Trp^{\bullet+}$. The final column shows the plots for the 15-nuclei cases magnified by a factor of 20 to show the different shapes but similar sizes of the anisotropy surface plots.

Figure 10 explores the effects on the magnetic sensitivity of systematically increasing the number of hyperfine-coupled nuclei in the $Trp^{\bullet+}$ radical. The eight nuclei in $FAD^{\bullet-}$ whose averaged hyperfine tensors have the largest root-mean-square eigenvalues (Table S1) were included in all cases. Nuclei in $Trp^{\bullet+}$ were added one at a time to produce the anisotropy surface plots in Fig. 10. First, the $Trp^{\bullet+}$ Hβ nuclei were considered because their average isotropic hyperfine couplings produce the greatest difference between the three RP states.

Nuclei were then added in the order N1, H1, H4, H2 and H6. For all three RP systems, the reaction yield anisotropy decreases considerably as more nuclei are added to $Trp^{\bullet+}$. This was also found in an earlier investigation[66] for *Drosophila* cryptochrome and by Kattnig *et al.*[27] for AtCry1 who noted that a RP containing only the two nitrogen atoms in $FAD^{\bullet-}$ shows a near-optimal magnetic sensitivity that is compromised by additional nuclei.

The anisotropy of the singlet yield is represented by the size of the surface plots in Fig. 10 and numerically by Γ. While ErD has the highest anisotropy in the first column of Fig. 10 (Γ(ErD) = 0.185, Γ(AtC) = 0.125, Γ(ErC) = 0.105), Γ drops drastically as more nuclei are added. With H1, H4, H2, and H6 included in $Trp^{\bullet+}$, all three RP systems have similar singlet yield anisotropies (Γ(AtC) = 0.003, Γ(ErC) = 0.002, Γ(ErD) = 0.003) (Table S3).

Figure 11 provides a final overview of the trends in Γ for all three RP states as the number of hyperfine interactions included in the calculation is increased (i.e. increasingly resembling the natural system). Hyperfine couplings from a single frame of the MD simulation (Fig. 11A) or averaged hyperfine couplings (Fig. 11B) were used. The number of $FAD^{\bullet-}$ nuclei is either 2, 5, or 8 (denoted 2hF, 5hF, 8hF), with the data shown in Fig. 10 corresponding to the first six data points in the 8hF lines in Fig. 11B.

Irrespective of the number of starting $FAD^{\bullet-}$ nuclei, Fig. 11B shows a similar trend. In each case, Γ decreases sharply when N1 and H1 are considered in $Trp^{\bullet+}$. However, this similarity ceases on addition of H4, H2, H6 etc. in $Trp^{\bullet+}$. In the 2hF case, the values of Γ for all three RPs converge to a similar value. For 8hF on the other hand Γ continues to decrease as H4, H2, H6 etc. are added sequentially.

Comparison of the results in Figs 11A and 11B reveals the very different values of Γ calculated using single-frame or averaged hyperfine interactions.

In Fig. 11A the RP in ErCry4a seems more sensitive to the magnetic field than that in AtC which could be wrongly attributed to variations in the librational angles and to a smaller extent the dihedral angles observed in the first part of the study. Thus, the differences

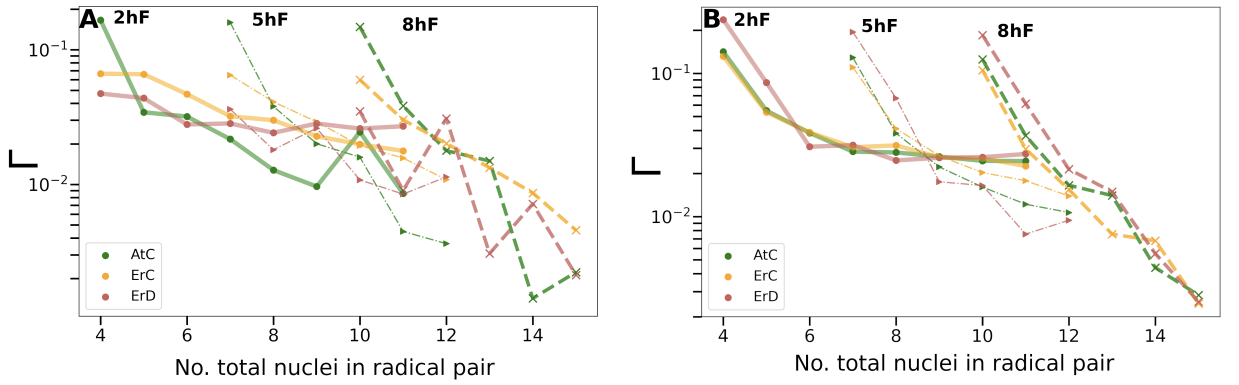

Figure 11: Singlet yield anisotropies calculated for RPs composed of different numbers of nuclei. **A**: Hyperfine couplings calculated using a single frame from the MD simulations. **B** Hyperfine interactions averaged over 1,200 ns. Each line style signifies RPs with the same number of nuclei in $FAD^{\bullet-}$. Solid lines: N5 and N10 (2hF). Point-dash lines: N5, N10, $H8_1$, $H8_2$ and $H8_3$ (5hF). Dashed lines: N5, N10, $H8_1$, $H8_2$, $H8_3$, H6, $H\beta_1$ and $H\beta_2$ (8hF). For $Trp^{\bullet+}$, each RP started with $H\beta_1$ and $H\beta_2$ and then N1, H1, H4, H2, H6, H7 and H5 were added one at a time in that order.

between Figs 11A and B highlight the importance of using motionally averaged interactions when studying compass sensitivity.

Conclusions

We have assessed the effects of protein dynamics on the performance of $FAD^{\bullet-}$ $Trp^{\bullet+}$ radical pairs as magnetic direction sensors in cryptochromes from a plant (AtCry1), a non-migratory bird (ClCry4a) and a migratory bird (ErCry4a). Hyperfine interactions in five radical pairs, AtC, ClC, ErC, ClD and ErD, were calculated using DFT based on structures sampled from extensive molecular dynamics simulations and used to compute the dependence of photochemical reaction yields on the direction of an Earth-strength magnetic field. The aim was to discover the extent and origin of any differences in magnetic sensitivity amongst the five systems.

The focus here has been on librational motions of the aromatic groups of the two radicals and fluctuations in the dihedral angles, Ω in $FAD^{\bullet-}$ and Λ in $Trp^{\bullet+}$ (Fig. 2), both of which

were anticipated to have a strong influence on the average hyperfine interactions. The main findings are (i) that there are larger fluctuations in $Trp^{\bullet+}$ than $FAD^{\bullet-}$ in all radical pairs considered, (ii) that the $Trp^{\bullet+}$ librations have a larger amplitude in AtCry1 than in ErCry4a and ClCry4a, and (iii) that the variations in the dihedral angles in both radicals are of similar amplitude in the three proteins. Differences in corresponding motions of different cryptochromes were also found. Although the structural similarity of ErCry4a and ClCry4a could imply similar dynamics of the two proteins, our simulations indicate that the behaviour of ClC is more similar to AtC than to ErC. This observation is particularly relevant if RPC is the main source of magnetic sensitivity in cryptochrome, as has been proposed.[25,34]

Apart from the different relative orientation in space, the principal difference between $TrpC^{\bullet+}$ and $TrpD^{\bullet+}$ is in the mean value of Λ reflecting the different environment of the two residues at the end of the Trp-tetrad. One consequence of these fluctuations is that the hyperfine interactions computed using single structures (e.g. as extracted from MD trajectories or crystal structures), and therefore the magnetic sensitivity of the reaction yields, can be very different from the time-averaged interactions and the corresponding magnetic field effects. Future attempts to assess the performance of radical pairs as compass sensors should therefore not be based on single snapshots of the protein structure.

The hyperfine interactions most strongly affected by the dynamics investigated here are those of the Hβ protons in both $FAD^{\bullet-}$ and $Trp^{\bullet+}$. An investigation of the latter showed that variations in Λ, which affect the extent of hyperconjugation between the indole group and the remainder of the $Trp^{\bullet+}$ sidechain, account for only a part of the spread in the Hβ couplings and that other structual variations of $Trp^{\bullet+}$ within the protein are at least as important. For radical pairs of comparable relative orientation[67] such as ErC and AtC, the differences in these Hβ hyperfine interactions have the largest effect on their differences in magnetic sensitivity. However, once large numbers of hyperfine-coupled nuclei are included in the spin dynamics simulations, the anisotropic magnetic field effects on AtC, ErC and

ErD are all of similar amplitude. This suggests that significant differences amongst the five radical pairs as a result of structural fluctuations are more likely to be found in simulations that include the time-dependence of the hyperfine interactions (via the spin relaxation they induce) than in calculations which consider instantaneous or time-averaged couplings. A computational comparison of spin relaxation effects in the three RPs is in progress.

Clearly, there are factors other than hyperfine interactions that can influence the performance of $FAD^{\bullet-}$ $Trp^{\bullet+}$ radical pairs in a cryptochrome. The different separations of the two radicals in ErC and ErD (roughly 1.8 nm and 2.1 nm, respectively) will affect the electron-electron dipolar coupling and the rate of return to the protein's ground state and hence the spin dynamics.[68–70] Variations in the environments of the radicals arising from sequence differences, e.g. for ErC compared to AtC, can change electron transfer rates and also the rate at which $Trp^{\bullet+}$ is stabilised by deprotonation.[25,27,71] Furthermore, the protonation kinetics of $FAD^{\bullet-}$ in ErCry4a and AtCry1 is expected to be significantly different, which will also influence the overall compass performance.[19]

In addition, there is the recently proposed possibility that $FAD^{\bullet-}$ $TrpC^{\bullet+}$ and $FAD^{\bullet-}$ $TrpD^{\bullet+}$ interconvert rapidly such that both RPs contribute to both the magnetic sensitivity and the efficiency of the initial events of signal transduction.[25,34] Clearly, this cannot occur in the plant protein which lacks TrpD. As well as a study of the differential effects of spin relaxation in the radical pairs, future work will focus on calculations of hyperfine interactions in which the $FAD^{\bullet-}$ and the Trp-tetrad and their immediate environment are modelled as a single quantum system.

The results presented here reveal the significant influence of motion on the hyperfine interactions in $FAD^{\bullet-}$ and $Trp^{\bullet+}$, which must be considered for a reliable simulation of RP spin dynamics in cryptochrome proteins, and the surprising realization that the cryptochromes of migratory birds are not more sensitive to a weak magnetic field if large spin systems are considered, at least based on the time-averaged hyperfine couplings. Thus, differences, if

they exist, will manifest as a consequence of structural fluctuations via the spin relaxation that they induce. The information obtained here on the dynamics of cryptochromes will be an essential precursor to future detailed investigations of the effects of spin relaxation in flavin-tryptophan radical pairs.

Supporting Information

Figures S1-S21 and Tables S1-S3 generated in the present study, exemplary input files for the hyperfine and quantum yield calculations and supplementary theoretical methods used in the present investigation (PDF).

Acknowledgements

We acknowledge the financial support of the Deutsche Forschungsgemeinschaft, project nos. 395940726 (SFB 1372, Magnetoreception and Navigation in Vertebrates) and GRK1885 (Molecular basis of sensory biology). I.A.S. thanks the Lundbeck Foundation and the Volkswagen Foundation (Lichtenberg Professorship) and the Ministry for Science and Culture of Lower Saxony ('Simulations meet experiments on the nanoscale: opening up the quantum world to artificial intelligence', SMART). Computational resources for the simulations were provided by the CARL Cluster at the Carl-von-Ossietzky University of Oldenburg and the North German Supercomputing Alliance (HLRN). P.J.H. is grateful to the European Research Council (under the European Union's Horizon 2020 research and innovation programme, grant agreement no.810002, Synergy Grant, QuantumBirds) and the Office of Naval Research Global (award no. N62909-19-1-2045). D.R.K. thanks the UK Defence Science and Technology Laboratory (Grant No. DSTLX-1000139168), the Office of Naval Research (ONR Award No. N62909-21-1-2018), and the EPSRC (Grant No. EP/V047175/1).

References

(1) Wiltschko, R.; Wiltschko, W. *Magnetic Orientation in Animals*, 1st ed.; Springer-Verlag: Berlin, 1995; pp 1–297.

(2) Wiltschko, R.; Thalau, P.; Gehring, D.; Niessner, C.; Ritz, T.; Wiltschko, W. Magnetoreception in birds: the effect of radio-frequency fields. *J. R. Soc. Interface* **2015**, *12*, 20141103.

(3) Mouritsen, H.; Ritz, T. Magnetoreception and its use in bird navigation. *Curr. Opin. Neurobiol.* **2005**, *15*, 406–414.

(4) Mouritsen, H. Navigation in birds and other animals. *Image Vis Comput* **2001**, *19*, 713–731.

(5) Spiecker, L.; Leberecht, B.; Langebrake, C.; Laurien, M.; Apte, S. R.; Mouritsen, H.; Gerlach, G.; Liedvogel, M. Endless skies and open seas – how birds and fish navigate. *Neuroforum* **2021**, *27*, 127–139.

(6) Wiltschko, W.; Wiltschko, R. Magnetic compass of European robins. *Science* **1972**, *176*, 62–64.

(7) Hiscock, H. G.; Worster, S.; Kattnig, D. R.; Steers, C.; Jin, Y.; Manolopoulos, D. E.; Mouritsen, H.; Hore, P. J. The quantum needle of the avian magnetic compass. *Proc. Natl. Acad. Sci. U.S.A.* **2016**, *113*, 4634–4639.

(8) Hore, P. J.; Mouritsen, H. The radical-pair mechanism of magnetoreception. *Annu. Rev. Biophys.* **2016**, *45*, 299–344.

(9) Hiscock, H. G.; Mouritsen, H.; Manolopoulos, D. E.; Hore, P. J. Disruption of magnetic compass orientation in migratory birds by radiofrequency electromagnetic fields. *Biophys. J.* **2017**, *113*, 1475–1484.

(10) Ritz, T.; Adem, S.; Schulten, K. A model for photoreceptor-based magnetoreception in birds. *Biophys. J.* **2000**, *78*, 707–718.

(11) Immeln, D.; Weigel, A.; Kottke, T.; Pérez Lustres, J. L. Primary events in the blue light sensor plant cryptochrome: Intraprotein electron and proton transfer revealed by femtosecond spectroscopy. *J. Am. Chem. Soc.* **2012**, *134*, 12536–12546.

(12) Kao, Y.-T.; Tan, C.; Song, S.-H.; Öztürk, N.; Li, J.; Wang, L.; Sancar, A.; Zhong, D. Ultrafast dynamics and anionic active states of the flavin cofactor in cryptochrome and photolyase. *J. Am. Chem. Soc.* **2008**, *130*, 7695–7701.

(13) Brazard, J.; Usman, A.; Lacombat, F.; Ley, C.; Martin, M. M.; Plaza, P.; Mony, L.; Heijde, M.; Zabulon, G.; Bowler, C. Spectro-temporal characterization of the photoactivation mechanism of two new oxidized cryptochrome/photolyase photoreceptors. *J. Am. Chem. Soc.* **2010**, *132*, 4935–4945.

(14) Martin, R.; Lacombat, F.; Espagne, A.; Dozova, N.; Plaza, P.; Yamamoto, J.; Müller, P.; Brettel, K.; de la Lande, A. Ultrafast flavin photoreduction in an oxidized animal (6-4) photolyase through an unconventional tryptophan tetrad. *Phys. Chem. Chem. Phys.* **2017**, *19*, 24493–24504.

(15) Lukacs, A.; Eker, A. P. M.; Byrdin, M.; Brettel, K.; Vos, M. H. Electron hopping through the 15 Å triple tryptophan molecular wire in DNA photolyase occurs within 30 ps. *J. Am. Chem. Soc.* **2008**, *130*, 14394–14395.

(16) Ritz, T.; Ahmad, M.; Mouritsen, H.; Wiltschko, R.; Wiltschko, W. Photoreceptor-based magnetoreception: optimal design of receptor molecules, cells, and neuronal processing. *J. R. Soc. Interface* **2010**, *7*, S135–S146.

(17) Lau, J.; Wagner-Rundell, N.; Rodgers, C.; Green, N.; Hore, P. J. Effects of disorder

and motion in a radical pair magnetoreceptor. *J. R. Soc. Interface* **2009**, *7 Suppl 2*, S257–S264.

(18) Solov'yov, I. A.; Mouritsen, H.; Schulten, K. Acuity of a cryptochrome and vision-based magnetoreception system in birds. *Biophys. J.* **2010**, *99*, 40–49.

(19) Maeda, K.; Robinson, A. J.; Henbest, K. B.; Hogben, H. J.; Biskup, T.; Ahmad, M.; Schleicher, E.; Weber, S.; Timmel, C. R.; Hore, P. J. Magnetically sensitive light-induced reactions in cryptochrome are consistent with its proposed role as a magnetoreceptor. *Proc. Natl. Acad. Sci. U.S.A.* **2012**, *109*, 4774–4779.

(20) Wu, H.; Scholten, A.; Einwich, A.; Mouritsen, H.; Koch, K.-W. Protein-protein interaction of the putative magnetoreceptor cryptochrome 4 expressed in the avian retina. *Sci. Rep.* **2020**, *10*, 7364.

(21) Görtemaker, K.; Yee, C.; Bartölke, R.; Behrmann, H.; Voß, J.-O.; Schmidt, J.; Xu, J.; Solovyeva, V.; Leberecht, B.; Behrmann, E.; Mouritsen, H.; Koch, K.-W. Direct Interaction of Avian Cryptochrome 4 with a Cone Specific G-Protein. *Cells* **2022**, *11*, 2043.

(22) Sheppard, D. M.; Li, J.; Henbest, K. B.; Neil, S. R.; Maeda, K.; Storey, J.; Schleicher, E.; Biskup, T.; Rodriguez, R.; Weber, S.; Hore, P. J.; Timmel, C. R.; MacKenzie, S. R. Millitesla magnetic field effects on the photocycle of an animal cryptochrome. *Sci. Rep.* **2017**, *7*, 1–7.

(23) Kattnig, D. R.; Evans, E. W.; Déjean, V.; Dodson, C. A.; Wallace, M. I.; Mackenzie, S. R.; Timmel, C. R.; Hore, P. J. Chemical amplification of magnetic field effects relevant to avian magnetoreception. *Nat. Chem.* **2016**, *8*, 384–391.

(24) Giovani, B.; Byrdin, M.; Ahmad, M.; Brettel, K. Light-induced electron transfer in a cryptochrome blue-light photoreceptor. *Nat. Struct. Mol. Biol* **2003**, *10*, 489–490.

(25) Xu, J. et al. Magnetic sensitivity of cryptochrome 4 from a migratory songbird. *Nature* **2021**, *594*, 535–540.

(26) Liedvogel, M.; Mouritsen, H. Cryptochromes - a potential magnetoreceptor: what do we know and what do we want to know? *J. R. Soc. Interface* **2010**, *7*, S147–S162.

(27) Kattnig, D. R.; Solov'yov, I. A.; Hore, P. J. Electron spin relaxation in cryptochrome-based magnetoreception. *Phys. Chem. Chem. Phys.* **2016**, *18*, 12443–12456.

(28) Strümpfer, J.; Şener, M.; Schulten, K. How quantum coherence assists photosynthetic light-harvesting. *J. Phys. Chem. Lett.* **2012**, *3*, 536–542.

(29) Chrysafoudi, A.; Maity, S.; Kleinekathöfer, U.; Daskalakis, V. Robust strategy for photoprotection in the light-harvesting antenna of diatoms: A molecular dynamics study. *J. Phys. Chem. Lett.* **2021**, *12*, 9626–9633.

(30) Maity, S.; Sarngadharan, P.; Daskalakis, V.; Kleinekathöfer, U. Time-dependent atomistic simulations of the CP29 light-harvesting complex. *J. Chem. Phys.* **2021**, *155*, 055103.

(31) Damjanović, A.; Kosztin, I.; Kleinekathöfer, U.; Schulten, K. Excitons in a photosynthetic light-harvesting system: A combined molecular dynamics, quantum chemistry, and polaron model study. *Phys. Rev. E* **2002**, *65*, 031919.

(32) Günther, A.; Einwich, A.; Sjulstok, E.; Feederle, R.; Bolte, P.; Koch, K. W.; Solov'yov, I. A.; Mouritsen, H. Double-cone localization and seasonal expression pattern suggest a role of magnetoreception for European robin cryptochrome 4. *Curr. Biol.* **2018**, *28*, 211–223.

(33) Wong, S. Y.; Frederiksen, A.; Hanić, M.; Schuhmann, F.; Grüning, G.; Hore, P. J.;

Solov'yov, I. A. Navigation of migratory songbirds: a quantum magnetic compass sensor. *Neuroforum* **2021**, *27*, 141–150.

(34) Wong, S. Y.; Wei, Y.; Mouritsen, H.; Solov'yov, I. A.; Hore, P. J. Cryptochrome magnetoreception: four tryptophans could be better than three. *J. R. Soc. Interface* **2021**, *18*, 20210601.

(35) Hanić, M.; Schuhmann, F.; Frederiksen, A.; Langebrake, C.; Manthey, G.; Liedvogel, M.; Xu, J.; Mouritsen, H.; Solov'yov, I. A. Computational reconstruction and analysis of structural models of avian Cryptochrome 4. *J. Phys. Chem. B* **2022**, *126*, 4623–4635.

(36) Hanić, M.; Frederiksen, A.; Schuhmann, F.; Solov'yov, I. A. On the energetic differences of avian cryptochromes 4 from selected species. *Eur. Phys. J. D* **2022**, *76*, 1–14.

(37) Brooks, C. L.; Case, D. A.; Plimpton, S.; Roux, B.; van der Spoel, D.; Tajkhorshid, E. Classical molecular dynamics. *J. Chem. Phys.* **2021**, *154*, 100401.

(38) Perilla, J. R.; Goh, B. C.; Cassidy, C. K.; Liu, B.; Bernardi, R. C.; Rudack, T.; Yu, H.; Wu, Z.; Schulten, K. Molecular dynamics simulations of large macromolecular complexes. *Curr. Opin. Struct. Biol.* **2015**, *31*, 64–74.

(39) Chandler, D. E.; Struempfer, J.; Sener, M.; Scheuring, S.; Schulten, K. Light harvesting by lamellar chromatophores in *Rhodospirillum photometricum*. *Biophys. J.* **2014**, *106*, 2503–2510.

(40) Gupta, P.; Liu, B.; Klepacki, D.; Gupta, V.; Schulten, K.; Mankin, A. S.; Vazquez-Laslop, N. Nascent peptide assists the ribosome in recognizing chemically distinct small molecules. *Nat. Chem. Biol.* **2016**, *12*, 153–158.

(41) DeMirci, H. et al. Intersubunit coupling enables fast CO_2-fixation by reductive carboxylases. *ACS Cent. Sci.* **2022**, *8*, 1091–1101.

(42) Deviers, J.; Cailliez, F.; Gutiérrez, B. Z.; Kattnig, D. R.; de la Lande, A. Ab initio derivation of flavin hyperfine interactions for the protein magnetosensor cryptochrome. *Phys. Chem. Chem. Phys.* **2022**, *24*, 16784–16798.

(43) Nielsen, C.; Solov'yov, I. A. MolSpin—Flexible and extensible general spin dynamics software. *J. Chem. Phys.* **2019**, *151*, 194105.

(44) Zoltowski, B. D.; Chelliah, Y.; Wickramaratne, A.; Jarocha, L.; Karki, N.; Xu, W.; Mouritsen, H.; Hore, P. J.; Hibbs, R. E.; Green, C. B.; Takahashi, J. S. Chemical and structural analysis of a photoactive vertebrate cryptochrome from pigeon. *Proc. Natl. Acad. Sci. U.S.A.* **2019**, *116*, 19449–19457.

(45) Phillips, J. C.; Braun, R.; Wan, W.; Gumbart, J.; Tajkhorshid, E.; Villa, E.; Chipot, C.; Skeel, R. D.; Kalé, L.; Schulten, K. Scalable molecular dynamics with NAMD. *J. Comput. Chem.* **2005**, *26*, 60–76.

(46) Phillips, J. C. et al. Scalable molecular dynamics on CPU and GPU architectures with NAMD. *J. Chem. Phys.* **2020**, *153*, 044130.

(47) Korol, V.; Husen, P.; Sjulstok, E.; Nielsen, C.; Friis, I.; Frederiksen, A.; Salo, A. B.; Solov'yov, I. Introducing VIKING: A novel online platform for multiscale modeling. *ACS Omega* **2020**, *5*, 1254–1260.

(48) Schuhmann, F.; Kattnig, D. R.; Solov'yov, I. A. Exploring post-activation conformational changes in pigeon cryptochrome 4. *J. Phys. Chem. B* **2021**, 9652–9659.

(49) MacKerell, A. D. et al. All-atom empirical potential for molecular modeling and dynamics studies of proteins. *J. Phys. Chem. B* **1998**, *102*, 3586–3616.

(50) MacKerell, A.; Feig, M.; Brooks, C. Extending the treatment of backbone energetics in protein force fields: Limitations of gas-phase quantum mechanics in reproducing protein conformational distributions in molecular dynamics simulations. *J. Comput. Chem.* **2004**, *25*, 1400–1415.

(51) Huang, J.; MacKerell Jr, A. D. CHARMM36 all-atom additive protein force field: Validation based on comparison to NMR data. *J. Comput. Chem.* **2013**, *34*, 2135–2145.

(52) Jorgensen, W. L.; Chandrasekhar, J.; Madura, J. D.; Impey, R. W.; Klein, M. L. Comparison of simple potential functions for simulating liquid water. *J. Chem. Phys.* **1983**, *79*, 926–935.

(53) Humphrey, W.; Dalke, A.; Schulten, K. VMD - Visual Molecular Dynamics. *J. Mol. Graph. Model.* **1996**, *14*, 33–38.

(54) Frisch, M. J. et al. Gaussian09 Revision D.01. **2013**, Gaussian Inc. Wallingford CT 2009.

(55) McLean, A. D.; Chandler, G. S. Contracted Gaussian basis sets for molecular calculations. I. Second row atoms, Z=11–18. *J. Chem. Phys.* **1980**, *72*, 5639–5648.

(56) Krishnan, R.; Binkley, J. S.; Seeger, R.; Pople, J. A. Self-consistent molecular orbital methods. XX. A basis set for correlated wave functions. *J. Chem. Phys.* **1980**, *72*, 650–654.

(57) Becke, A. D. Density-functional thermochemistry. III. The role of exact exchange. *J. Chem. Phys.* **1993**, *98*, 5648–5652.

(58) Barone, V. *Recent advances in density functional methods*; Chong, D. P.; World Scientific: Singapore, 1995; pp 287–334.

(59) Brautigam, C. A.; Smith, B. S.; Ma, Z.; Palnitkar, M.; Tomchick, D. R.; Machius, M.; Deisenhofer, J. Structure of the photolyase-like domain of cryptochrome 1 from *Arabidopsis thaliana*. *Proc. Natl. Acad. Sci. U.S.A.* **2004**, *101*, 12142–12147.

(60) Liedvogel, M.; Maeda, K.; Henbest, K.; Schleicher, E.; Simon, T.; Timmel, C. R.; Hore, P. J.; Mouritsen, H. Chemical magnetoreception: Bird cryptochrome 1a is excited by blue light and forms long-lived radical-pairs. *PLoS One* **2007**, *2*, 1–7.

(61) Rodgers, C. T.; Hore, P. J. Chemical magnetoreception in birds: The radical pair mechanism. *Proc. Natl. Acad. Sci. USA* **2009**, *106*, 353–360.

(62) Dai, S. Simple derivation of the Heller-McConnell equation. *J. Chem. Educ.* **1991**, *68*, 894.

(63) Heller, C.; McConnell, H. M. Radiation damage in organic crystals. II. Electron spin resonance of $(CO_2H)CH_2CH(CO_2H)$ in β-Succinic Acid. *J. Chem. Phys.* **1960**, *32*, 1535–1539.

(64) Atherton, N. M. In *Electron spin resonance; theory and applications*; Horwood, E., Ed.; Halsted Press: Chichester, 1973; pp 104–108.

(65) Wong, S. Y.; Solov'yov, I. A.; Hore, P. J.; Kattnig, D. R. Nuclear polarization effects in cryptochrome-based magnetoreception. *J. Chem. Phys.* **2021**, *154*, 035102.

(66) Lee, A. A.; Lau, J. C.; Hogben, H. J.; Biskup, T.; Kattnig, D. R.; Hore, P. J. Alternative radical pairs for cryptochrome-based magnetoreception. *J. R. Soc. Interface* **2014**, *11*, 20131063.

(67) Atkins, C.; Bajpai, K.; Rumball, J.; Kattnig, D. R. On the optimal relative orientation of radicals in the cryptochrome magnetic compass. *J. Chem. Phys.* **2019**, *151*, 065103.

(68) Kattnig, D. R.; Sowa, J. K.; Solov'yov, I. A.; Hore, P. J. Electron spin relaxation can enhance the performance of a cryptochrome-based magnetic compass sensor. *New J. Phys.* **2016**, *18*, 063007.

(69) Babcock, N. S.; Kattnig, D. R. Electron–electron dipolar interaction poses a challenge to the radical pair mechanism of magnetoreception. *J. Phys. Chem* **2020**, *11*, 2414–2421.

(70) Babcock, N. S.; Kattnig, D. R. Radical scavenging could answer the challenge posed by electron–electron dipolar interactions in the cryptochrome compass model. *J. Am. Chem. Soc.* **2021**, *1*, 2033–2046.

(71) Solov'yov, I. A.; Chandler, D. E.; Schulten, K. Magnetic field effects in *Arabidopsis thaliana* cryptochrome-1. *Biophys. J.* **2007**, *92*, 2711–2726.

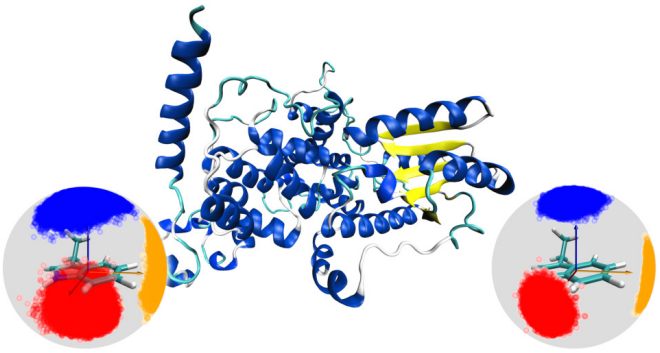

Figure 12: For Table of Contents Only

The effects of dynamical degrees of freedom on magnetic compass sensitivity: A comparison of plant and avian cryptochromes (Supplementary Material)

Gesa Grüning,[*,†] Siu Ying Wong,[†] Luca Gerhards,[†] Fabian Schuhmann,[†] Daniel R. Kattnig,[‡] P. J. Hore,[¶] and Ilia A. Solov'yov[*,†,§,‖]

†*Department of Physics, Carl von Ossietzky University, Carl-von-Ossietzky-Str. 9-11, 26129 Oldenburg, Germany*

‡*Department of Physics and Living Systems Institute, University of Exeter, Stocker Road, Exeter, EX4 4QD, United Kingdom*

¶*Department of Chemistry, University of Oxford, Physical and Theoretical Chemistry Laboratory, Oxford, OX1 3QZ, United Kingdom*

§*Research Center for Neurosensory Science, Carl von Ossietzky Universität Oldenburg, 26111 Oldenburg, Germany*

‖*Center for Nanoscale Dynamics (CENAD), Carl von Ossietzky Universität Oldenburg, Institut für Physik, Ammerländer Heerstr. 114-118, 26129 Oldenburg, Germany*

E-mail: gesa.gruening@uni-oldenburg.de; ilia.solovyov@uni-oldenburg.de

Contents

1 Spin dynamics calculations

The stochastic Liouville equation,

$$-\frac{d\hat{\rho}(t)}{dt} = \frac{i}{\hbar}[\hat{\mathrm{H}}, \hat{\rho}(t)] + \hat{\hat{\kappa}}(t), \tag{S1}$$

describes the time evolution of the spin density operator $\hat{\rho}(t)$ of the radical pair resulting from the interactions specified in the spin Hamiltonian $\hat{\mathrm{H}}$ and the reaction superoperator $\hat{\hat{\kappa}}(t)$ which accounts for the spin-selective reactivity of the radical pairs (following the Haberkorn approach) defined as:

$$\hat{\hat{\kappa}}(t) = \sum_{j=\mathrm{S,T}} \frac{k_j}{2}(\hat{\mathrm{P}}_\mathrm{j}\hat{\rho}(t) + \hat{\rho}(t)\hat{\mathrm{P}}_\mathrm{j}). \tag{S2}$$

Here, S and T signify the singlet and the triplet states respectively, k_j denotes the rate constant of spin state j and $\hat{\mathrm{P}}_\mathrm{j}$ projects onto state j. In this study, only the Zeeman and hyperfine interactions were included in $\hat{\mathrm{H}}$ which can therefore be written:

$$\hat{\mathrm{H}} = \sum_{i=1}^{2}(\omega_0 \cdot \hat{\mathbf{S}}_i + \sum_{n_i} \hat{\mathbf{I}}_{i,n_i} \cdot \mathbf{A}_{i,n_i} \cdot \hat{\mathbf{S}}_i). \tag{S3}$$

The first term describes the Zeeman interaction of radical i with the external magnetic field $\mathbf{B}$ with ω_0 depending on the Bohr magneton, μ_B, as

$$\omega_0 = \frac{2.0023\mu_\mathrm{B}|\mathbf{B}|}{\hbar}. \tag{S4}$$

$\hat{\mathbf{S}}_i$ in Eq. (S3) is the electron spin operator for radical i. The second term in Eq. (S3) is the hyperfine interaction that includes the interaction of the n-th nuclear spin in radical i with the electronic spin through the operator $\hat{\mathbf{I}}_{i,n_i}$ and the hyperfine tensor $\mathbf{A}_{i,n_i}$.

2 Distributions of librational and dihedral angles

2.1 Mathematical modelling of the distributions

The variation in the librational angles around the molecular axes of $FAD^{\bullet-}$ and $Trp^{\bullet+}$ is well approximated by fitting Rayleigh distributions[1] to the data (see Fig. 3). The probability density function for the distribution is defined as:

$$f(x;\sigma_{\mathrm{S}}) = \frac{x}{\sigma_{\mathrm{S}}^2}\exp\left(-\frac{x^2}{2\sigma_{\mathrm{S}}^2}\right), \tag{S5}$$

for librational angles $x \geq 0$ with σ_{S} being the mode of the distribution. The dihedral angles Λ and Ω (Fig. 2) were fitted with a Gaussian distribution, defined as

$$f(x;\sigma) = \frac{1}{\sigma\sqrt{2\pi}}\exp\left(-\frac{1}{2}\left(\frac{x-\mu}{\sigma}\right)^2\right), \tag{S6}$$

where μ is the mean and σ the standard deviation of the distribution.

2.2 Translating the librational angles to a Cartesian coordinate system for the scatter plots in Fig. 3

To study the librational motion of the protein, the three MD simulation trajectories of the different RPs were aligned using VMD with respect to the backbone Cα atom positions in the first frame of the corresponding simulation.[2] This procedure is explained in an earlier study.[3]

For the creation of the librational angle scatter plots in Fig. 3A and Fig. 3C the coordinates from the atoms forming the central aromatic ring in the isoalloxazine group of $FAD^{\bullet-}$ and the indole ring in $Trp^{\bullet+}$ were extracted from the aligned trajectories and used to define the molecular coordinate systems of $FAD^{\bullet-}$ and $Trp^{\bullet+}$.

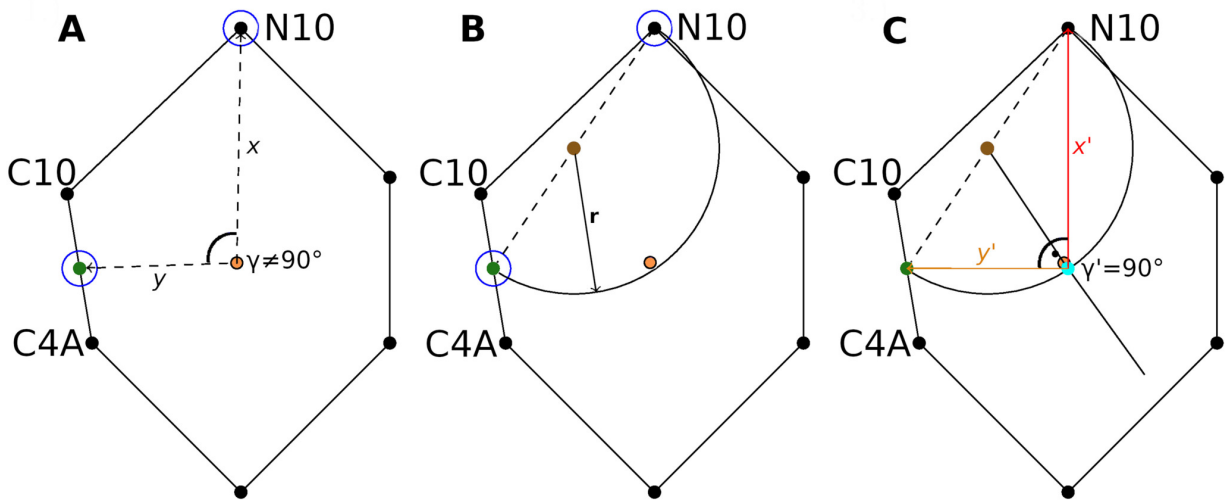

Figure S1: **A**: The central aromatic ring in the flavin with its geometric centre (orange dot) used as the origin of the molecular coordinate system. The atomic coordinates of N10, C10 and C4A are used to define the x- and y-axes for librational motion in $FAD^{\bullet-}$. The angle γ between the x- and y-axes may deviate from 90° making the coordinate system non-Cartesian. **B**: A line segment is constructed from N10 to the point defined as $\frac{\text{C10+C4A}}{2}$ (green dot) and a semi-circle with a radius **r** around the middle of the line segment (brown dot) is constructed. **C**: A line is drawn through the original geometric centre of the aromatic ring (orange dot) and the centre of the semicircle. The intersection of this line and the semi-circle (light blue dot) delivers, by Thales' theorem, a right angle between the x'- and y'-axes. This intersection point is chosen as the new origin of a Cartesian coordinate system and all atomic positions are translated with respect to the new origin.

The orange dot in Fig. S1A is the geometric centre of the central aromatic ring of the flavin composed of the atoms N10, N5, C9A, C10, C5A and C4A. For the $FAD^{\bullet-}$ the x-axis is defined as the line connecting the geometric centre of the ring and the N10 atom. The y-axis is the line connecting the geometric centre and the green point in the middle of the C4A-C10-bond (see Fig. S1A). The z-axis is orthogonal to the xy-plane. While projecting the librational angles of $FAD^{\bullet-}$ and $Trp^{\bullet+}$ onto the surface of a sphere a problem arises because the angle γ between the x- and y-axes may be not 90° which leads to the coordinate system spanned by the molecular axes being non-Cartesian. The bending motion of the aromatic rings in $FAD^{\bullet-}$ in every frame of the MD trajectory aggravates the problem because γ additionally acquires a different value in each frame. Scatter plots, such as Fig.

3A before corrections, therefore appear to contain points that fall away from the surface of the unit sphere. A procedure to transfer the librational angles extracted at each simulation time-step to a Cartesian coordinate system is applied by employing Thales' theorem[4] (see Fig. S1).

Thales' theorem states that for every two-dimensional line segment, a semicircle can be constructed, which passes through both ends of the line segment. If one chooses an arbitrary point on the semicircle and draws the triangle incorporating the line segment, it will always form a right-angled triangle.

In our case, first, the three points (positions of the N10, C10, C4A atoms) that are chosen to define the xy-plane of $FAD^{\bullet-}$, see Fig. S1A, are rotated so that the z-direction becomes redundant and Thales' theorem can be applied in two dimensions. Second, a half circle is constructed connecting the endpoints of the line segment between the position of N10 and the mid-point of the C4A-C10-bond (green dot) (Fig. S1B). Third, the centre of the aromatic ring has to be shifted to lie on the half circle (Fig. S1C). The translation guarantees that the x'- and y'-axes form a right angle. The z'-axis is constructed by taking the cross product of the unit vectors of the x'- and y'-axes. The normalized unit vectors along the newly defined x'-, y', and z'-axes yield an orthonormal (Cartesian) coordinate system. This coordinate transformation provides comparability of the angles extracted from all frames from the MD simulations and was used to project the dots in the scatter plots shown in Fig. 3A onto the surface of a unit sphere.

For $Trp^{\bullet+}$, the procedure of transferring the librational angles in each frame to a Cartesian coordinate system is analogous and was used to produce the data shown in Fig. 3C.

2.3 Distributions of dihedral angles in the MD simulations

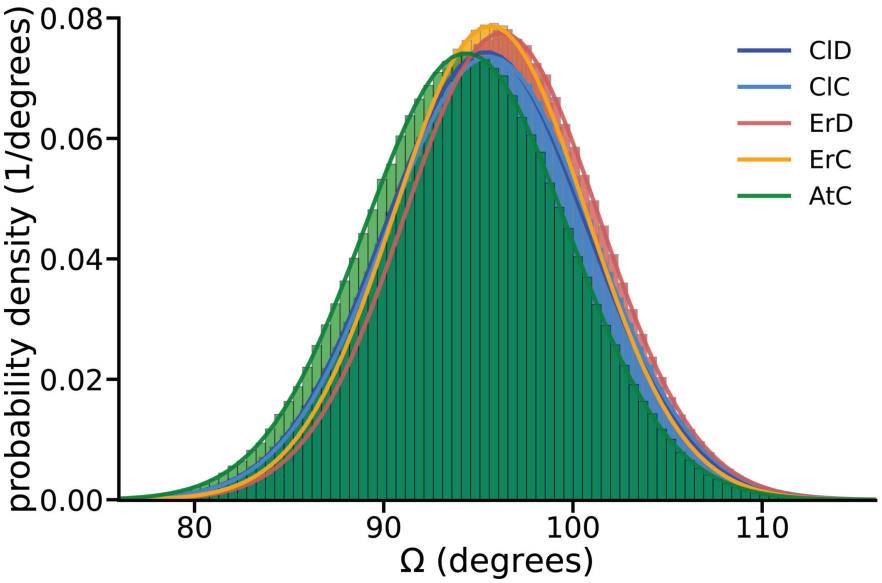

Figure S2: Probability distributions computed from the 2,400,000 values of the dihedral angle Ω extracted from the cumulative 1200 ns MD simulation for each RP state (AtC (green), ClC (light blue), ErC (orange), ClD (blue) and ErD (red)) shown together with the corresponding Gaussian fits (solid lines) computed with Eq. (S6).

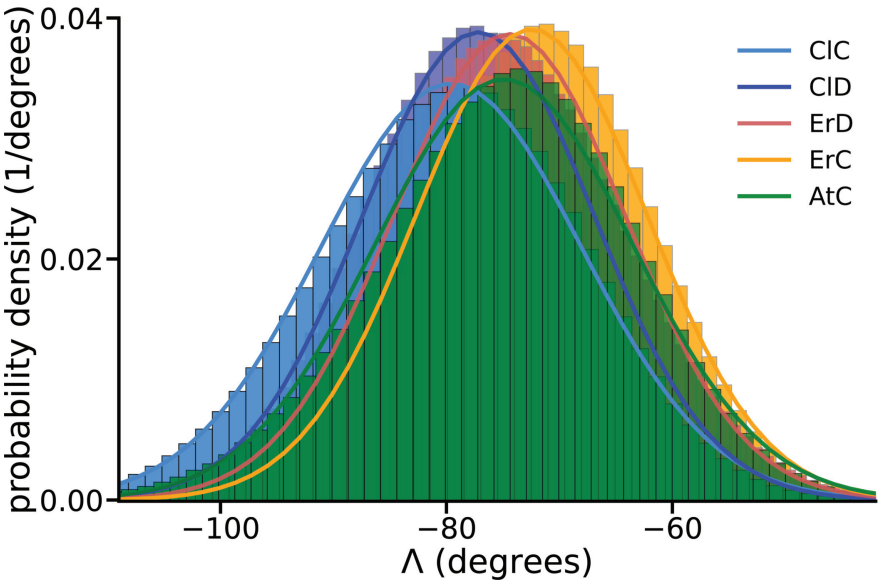

Figure S3: Probability distributions computed from the 2,400,000 values of the dihedral angle Λ extracted from the cumulative 1200 ns MD simulation for each RP state (AtC (green), ClC (light blue), ErC (orange), ClD (blue) and ErD (red)) shown together with the corresponding Gaussian fits (solid lines) computed with Eq. (S6). The distributions for Λ in ClD and ErD have been shifted by -150° for a better comparability with AtC, ClC and ErC.

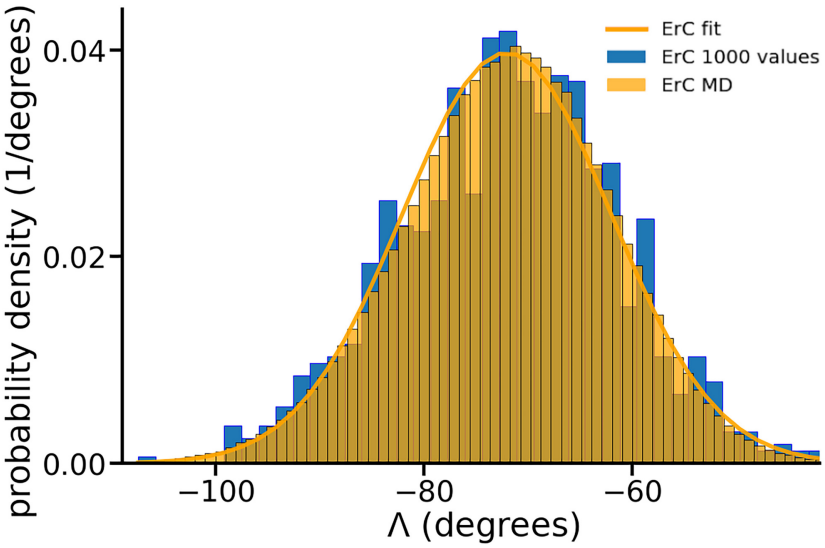

Figure S4: Probability distribution computed from the 2,400,000 values of the dihedral angle Λ extracted from the cumulative 1200 ns MD simulation for ErC (orange bars). The blue bars show the probability distribution obtained from the 1000 dihedral values computed from the MD snapshots taken 1.2 ns apart. The solid line shows the Gaussian fit (Eq. (S6)) to the data obtained from the simulation.

2.4 Distributions of librational angles in the MD simulations

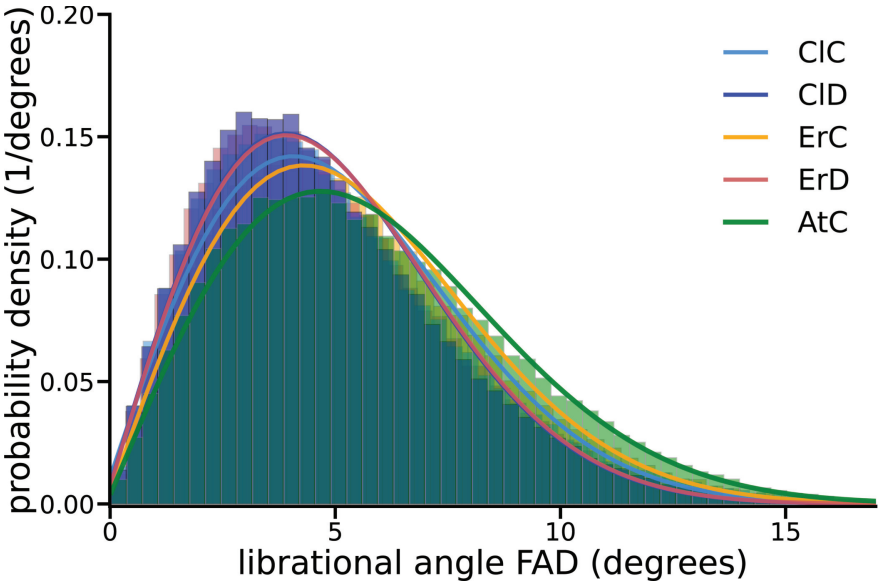

Figure S5: Probability distributions of the librational angles formed with the x-axis in $FAD^{\bullet-}$ defined in Fig. 3. Results for AtC, ClC, ErC, ClD and ErD were computed in the course of the 400 ns MD trajectory are shown together with the corresponding Rayleigh fits computed with Eq. (S5).

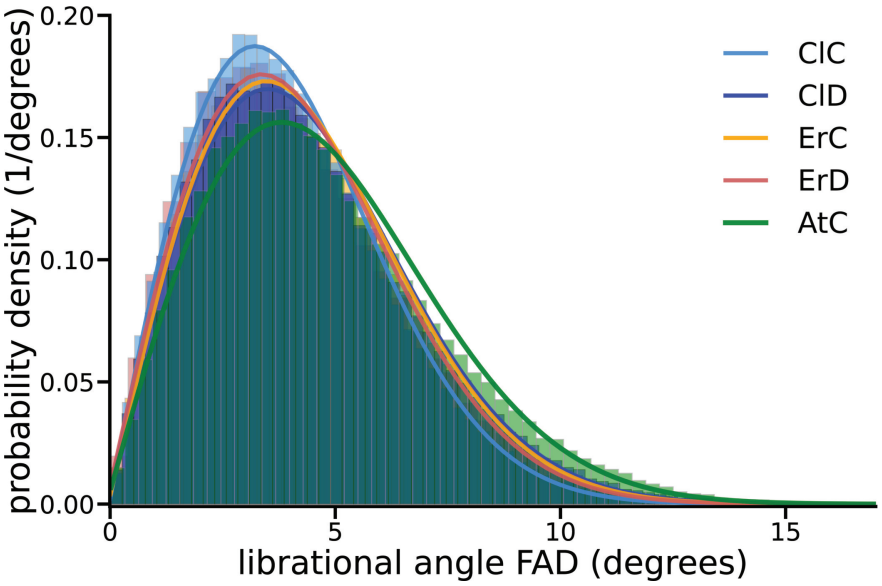

Figure S6: Probability distributions of the librational angles formed with the y-axis in $FAD^{\bullet-}$ defined in Fig. 3. Results for AtC, ClC, ErC, ClD and ErD were computed in the course of the 400 ns MD trajectory are shown together with the corresponding Rayleigh fits computed with Eq. (S5).

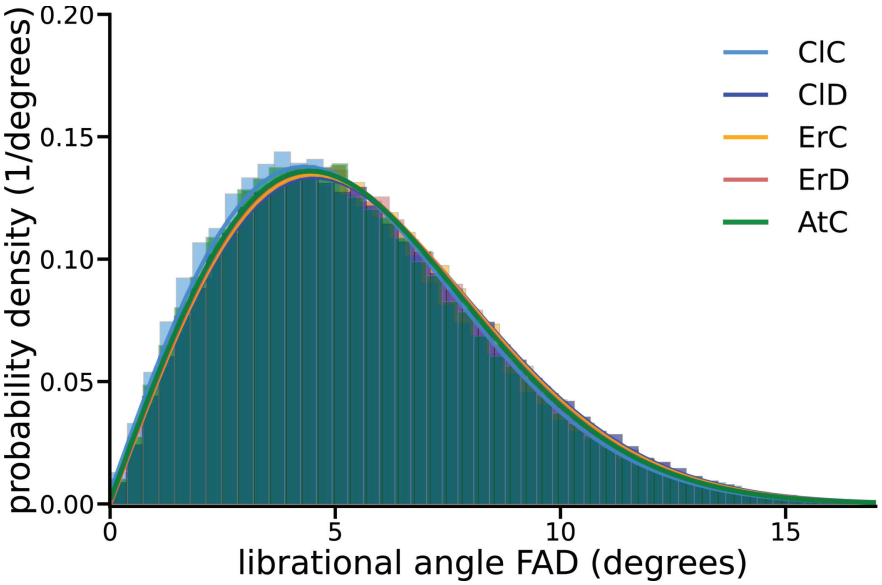

Figure S7: Probability distributions of the librational angles formed with the z-axis in $FAD^{\bullet-}$ defined in Fig. 3. Results for AtC, ClC, ErC, ClD and ErD were computed in the course of the 400 ns MD trajectory are shown together with the corresponding Rayleigh fits computed with Eq. (S5).

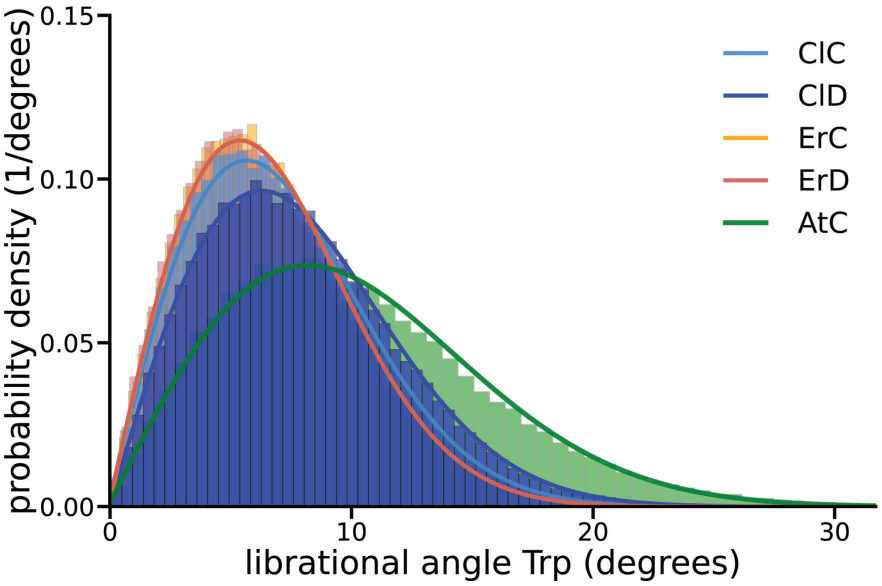

Figure S8: Probability distributions of the librational angles formed with the x-axis in $Trp^{\bullet+}$ defined in Fig. 3. Results for AtC, ClC, ErC, ClD and ErD were computed in the course of the 400 ns MD trajectory are shown together with the corresponding Rayleigh fits computed with Eq. (S5).

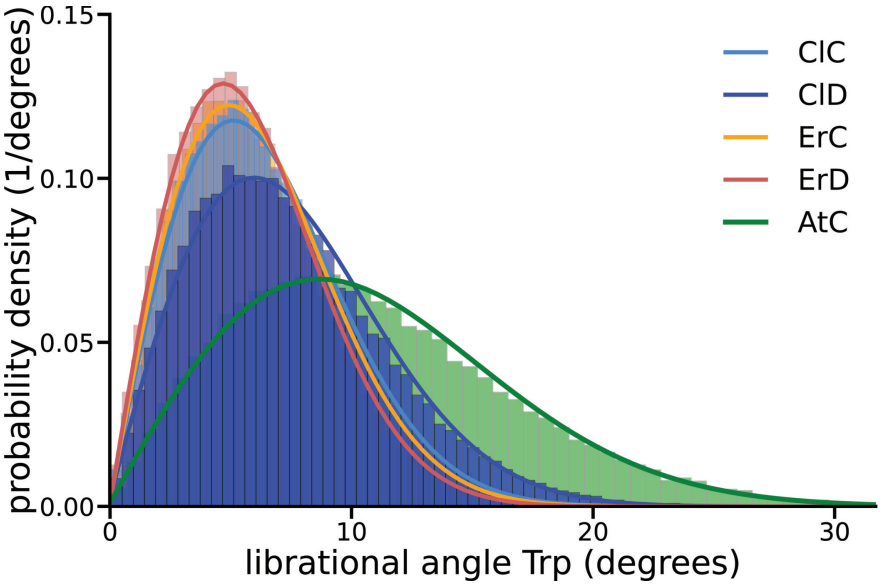

Figure S9: Probability distributions of the librational angles formed with the y-axis in $Trp^{\bullet+}$ defined in Fig. 3. Results for AtC, ClC, ErC, ClD and ErD were computed in the course of the 400 ns MD trajectory are shown together with the corresponding Rayleigh fits computed with Eq. (S5).

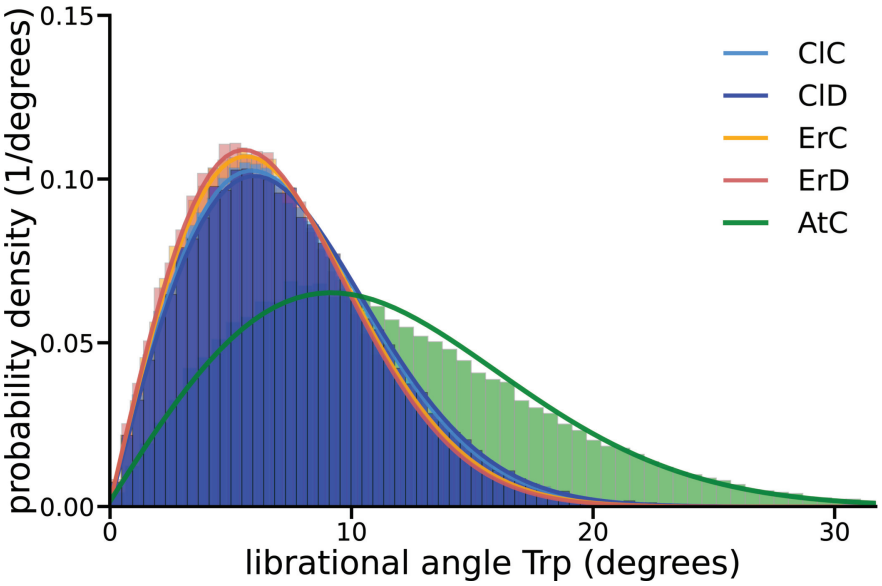

Figure S10: Probability distributions of the librational angles formed with the z-axis in $Trp^{\bullet+}$ defined in Fig. 3. Results for AtC, ClC, ErC, ClD and ErD were computed in the course of the 400 ns MD trajectory are shown together with the corresponding Rayleigh fits computed with Eq. (S5).

3 Hyperfine coupling

3.1 Hyperfine coupling calculation

```
%nprocshared=32
%mem=40GB
%chk=FAD_RPC_frame0opt_chk
# b3lyp/6-31G(d) Opt=ReadOpt

jobname_opFAD_frame(0)

-1 2
N 79.959 -39.197 69.063
C 79.83 -37.933 69.510
O 80.609 -37.024 69.147
N 79.006 -37.665 70.473
H 79.069 -36.766 70.929
C 78.107 -38.512 70.979
O 77.349 -38.062 71.869
C 78.089 -39.956 70.449
N 77.238 -40.954 70.819
C 77.239 -42.083 70.181
C 76.361 -43.093 70.634
H 75.549 -42.762 71.281
C 76.55 -44.385 70.293
C 75.296 -45.305 70.429
H 74.443 -44.995 71.070
H 75.595 -46.258 70.915
H 74.87 -45.412 69.408
C 77.594 -44.754 69.529
C 77.729 -46.167 69.004
H 77.255 -46.366 68.019
H 77.153 -46.881 69.632
H 78.765 -46.565 68.945
C 78.389 -43.851 68.980
H 79.169 -44.357 68.412
C 78.288 -42.498 69.315
N 79.201 -41.527 68.890
C 79.093 -40.197 69.419
C 80.284 -41.912 67.945
H 79.828 -42.628 67.228
H 80.572 -41.031 67.333
C 81.519 -42.466 68.595
H 82.232 -42.763 67.797
O 81.273 -43.669 69.237
H 82.009 -43.62 69.852
C 82.346 -41.477 69.509
H 81.656 -41.251 70.351
O 82.583 -40.274 68.717
H 81.754 -39.791 68.692
C 83.644 -41.94 70.056
H 84.174 -42.265 69.136
O 83.389 -43.124 70.941
H 84.268 -43.257 71.304
C 84.203 -40.7 70.783
H 84.487 -39.887 70.080
H 83.341 -40.452 71.440
O 85.286 -41.049 71.611
H 86.596 -41.698 71.036

atoms=47 notatoms=1-46

--Link1--
%chk=FAD_RPC_frame0opt_chk
%nprocshared=32
%mem=40GB
#P nmr=giao b3lyp/epr-ii Guess=Read Geom=(AllCheck,printinputorient)
```

Listing 1: Exemplary input file for the hyperfine coupling calculations in $FAD^{\bullet -}$ in ErC using Gaussian09.[5]

```
%nprocshared=32
%mem=20GB
%chk=TrpC_RPC_frame0opt_chk
# b3lyp/6-31G(d) Opt=ReadOpt

jobname_opTrpC_frame(0)

1 2
H 57.964 -49.14 68.319
C 58.874 -49.119 69.515
H 59.572 -49.943 69.543
C 59.726 -47.86 69.513
H 59.063 -46.97 69.464
H 60.207 -47.877 70.514
C 60.737 -47.758 68.339
C 60.758 -46.825 67.361
H 60.35 -45.83 67.456
N 61.731 -47.118 66.460
H 62.046 -46.564 65.721
C 62.327 -48.265 66.805
C 61.778 -48.711 68.053
C 62.214 -49.859 68.716
H 61.764 -50.235 69.623
C 63.194 -50.606 68.076
H 63.531 -51.555 68.467
C 63.426 -48.964 66.268
H 63.956 -48.646 65.382
C 63.791 -50.15 66.866
H 64.586 -50.789 66.510
H 58.038 -49.338 70.788

atoms=1,22 notatoms=2-21

--Link1--
%chk=TrpC_RPC_frame0opt_chk
%nprocshared=32
%mem=20GB
#P nmr=giao b3lyp/epr-ii Guess=Read Geom=(AllCheck,printinputorient)
```

Listing 2: Exemplary input file for the hyperfine coupling calculations in $Trp^{\bullet+}$ in ErC using Gaussian09.[5]

3.2 Distributions of isotropic hyperfine coupling constants

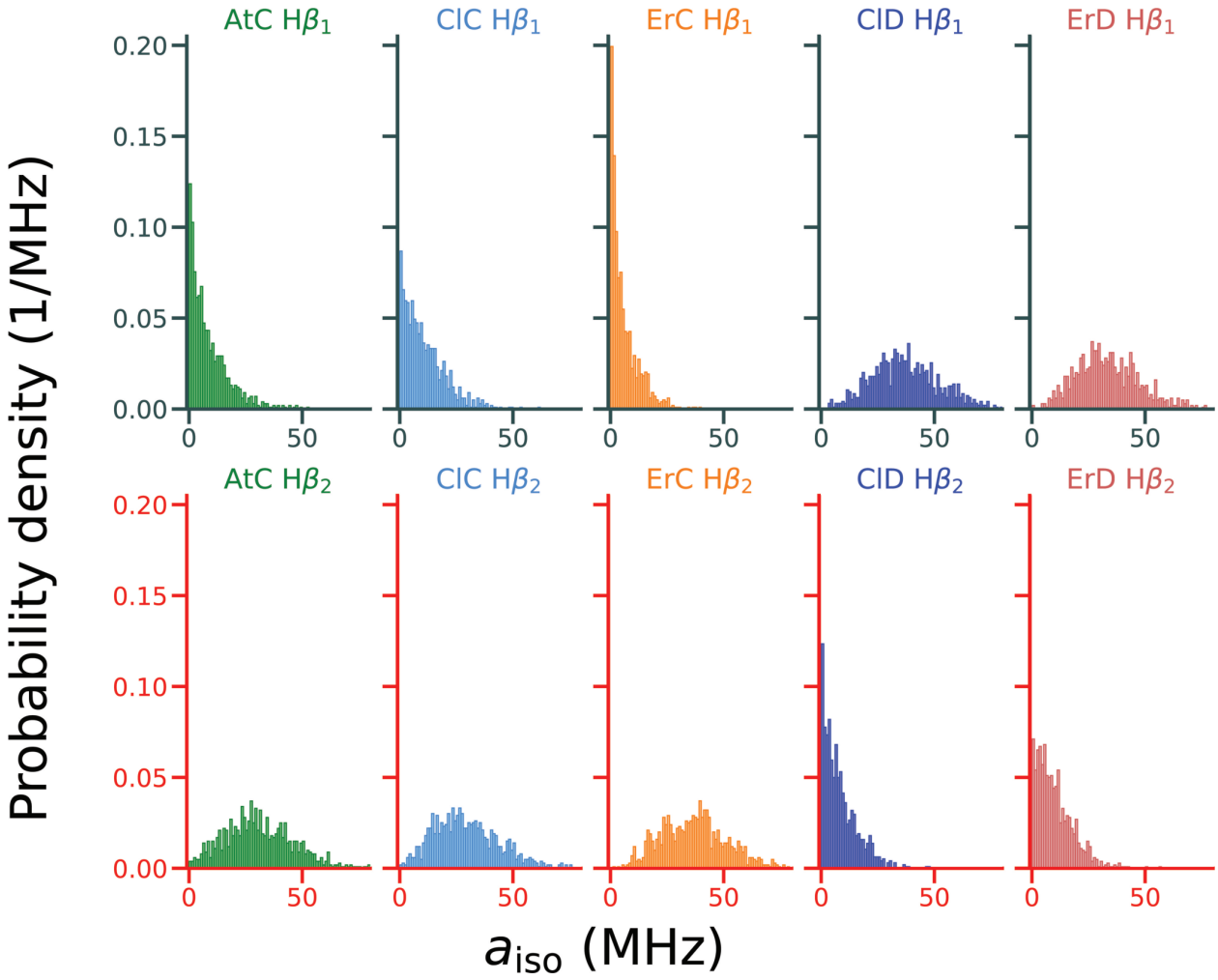

Figure S11: Distributions of the isotropic hyperfine coupling constants (in MHz) obtained for Hβ_1 and Hβ_2 in $Trp^{\bullet+}$ in AtC, ClC, ErC, ClD and ErD. Each distribution was calculated from the 1000 individual DFT calculations for structures taken at 1.2 ns intervals from the three 400-ns long MD simulations for each RP system. Each histogram covers a cumulative simulation time span of 1200 ns.

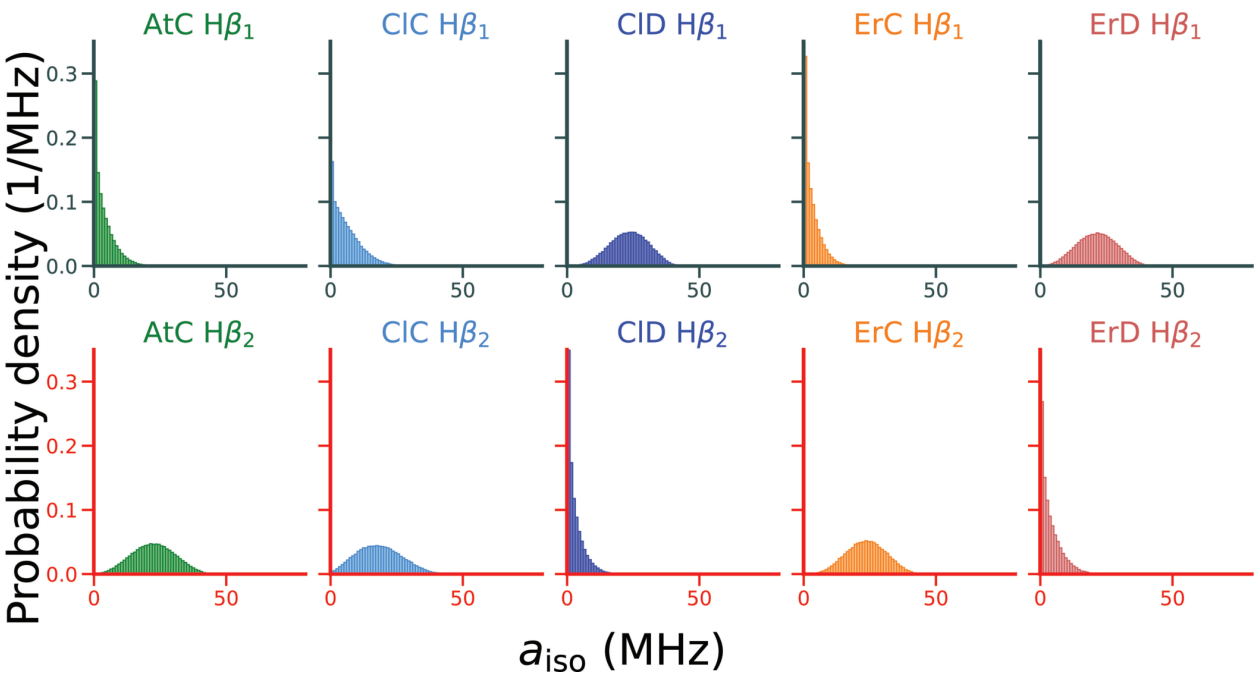

Figure S12: Expected distributions of the isotropic hyperfine coupling constants (in MHz) for Hβ1 and Hβ2 in $Trp^{\bullet+}$ in AtC, ClC, ErC, ClD and ErD, generated from the data shown in Fig. 6 by sampling the dark green and red curves of the Λ-dependent isotopic hyperfine coupling according to the three Gaussian-fitted distributions of Λ. Each Λ-distribution was calculated from the 2,400,000 Λ values covering a cumulative simulation time of 1200 ns. The shown distributions calculated solely on the basis of the Λ-distributions do not match the isotropic distributions of the values extracted from the MD simulation (Fig. S11) indicating, that the isotropic Hβ hyperfine couplings in the MD simulations depend on dynamical parameters other than just the Λ configurations.

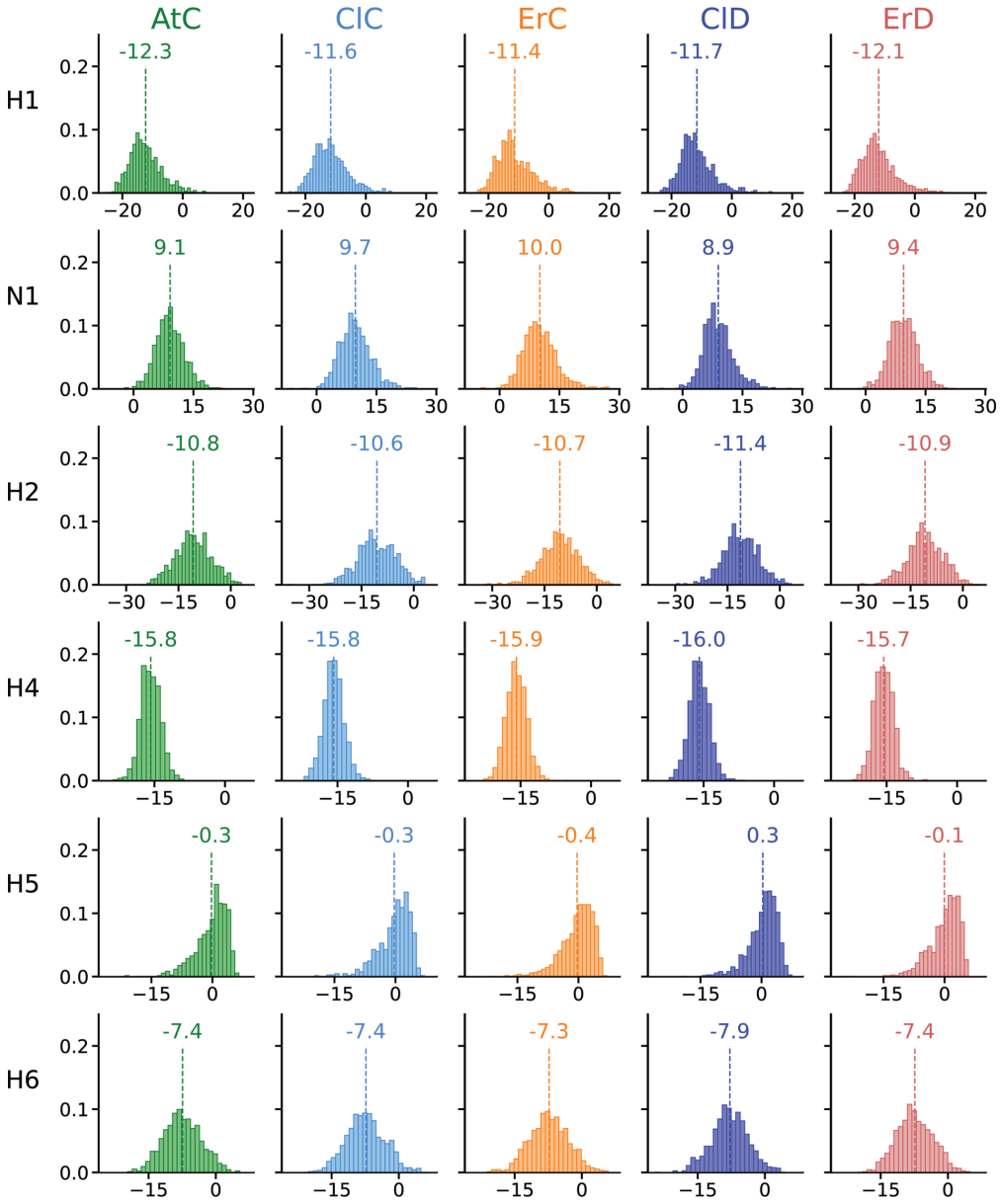

Figure S13: Probability distributions of the isotropic hyperfine coupling constants of H1, N1, H2, H4, H5 and H6 in $Trp^{\bullet+}$ in AtC, ClC, ErC, ClD and ErD. Each distribution was calculated from the 1,000 individual DFT calculations for structures taken at intervals of 1.2 ns from all of the three 400-ns long MD simulations for each RP system. Each histogram therefore covers a cumulative simulation time of 1200 ns. The dashed vertical lines indicate the mean isotropic hyperfine coupling of the distributions.

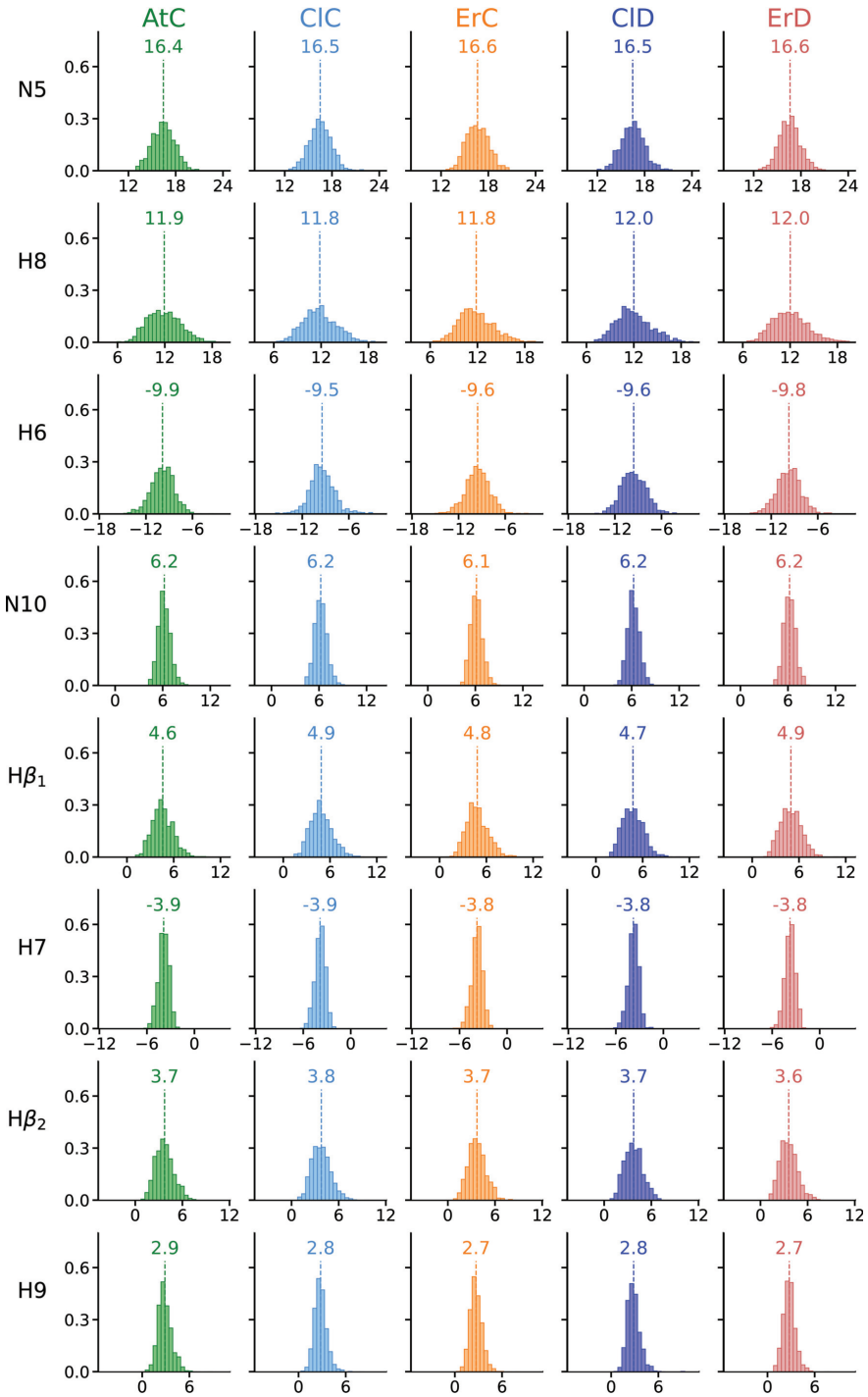

Figure S14: Probability distributions of the isotropic hyperfine coupling constants of N5, H8, H6, N10, Hβ_1, Hβ_1, H7 and H9 in FAD$^{\bullet-}$ in AtC, ClC, ErC, ClD and ErD. Each distribution was calculated from the 1,000 individual DFT calculations for structures taken at intervals of 1.2 ns from all of the three 400-ns long MD simulations for each RP system. Each histogram therefore covers a cumulative simulation time of 1200 ns. The dashed vertical lines indicate the mean isotropic hyperfine coupling of the distributions.

3.3 Principal values of the average hyperfine tensors

Table S1: Principal values of the average hyperfine tensors (in MHz) computed for the nuclei in $Trp^{\bullet+}$ transformed into the reference frame of $Trp^{\bullet+}$.

nuclei	AtC[3] (MHz)	AtC (MHz)	ErC (MHz)	ErD (MHz)
	4.3	6.5	3.5	30.6
$H\beta_1$	5.0	7.3	4.3	32.7
	10.0	12.7	9.8	36.5
	27.6	28.3	34.4	7.6
$H\beta_2$	28.8	30.0	36.1	8.8
	33.2	34.0	40.3	13.8
	-21.5	-18,0	-17.9	-18.2
H2	-16.0	-13.6	-13.4	-13.7
	-3.8	-0.9	-0.7	-0.9
	-1.5	0.0	0.9	27.1
N1	-1.3	0.8	1.5	1.0
	17.4	26.6	27.7	0.2
	-20.7	-24.6	-23.6	-24.6
H1	-15.3	-15.4	-14.7	-15.2
	-0.8	3.1	4.2	3.6
	-21.9	-23.9	-24.0	-23.6
H4	-17.1	-17.6	-17.7	-17.5
	-6.5	-5.9	-6.0	-5.9
	0.7	-2.2	-2.3	-2.0
H5	1.8	-1.7	-1.9	-1.5
	4.5	3.1	3.0	3.2
	-8.5	-15.2	-15.0	-14.7
H7	-7.5	-12.0	-11.8	-11.7
	-1.2	-2.6	-2.5	-2.5
	-15.4	-12.3	-12.2	-12.4
H6	-11.0	-9.0	-8.9	-9.0
	-3.2	-1.0	-1.0	-1.0

Table S2: Principal values of the average hyperfine tensors (in MHz) computed for the nuclei in $FAD^{\bullet-}$ transformed into the reference frame of $FAD^{\bullet-}$.

nuclei	AtC[3] (MHz)	AtC (MHz)	ErC (MHz)	ErD (MHz)
		-0.5	-0.6	-0.6
N1		-0.4	-0.5	-0.4
		1.0	0.9	0.9
		-1.8	-1.8	-1.7
N3		-1.1	-1.1	-1.1
		-0.9	-0.9	-0.9
		-1.3	-1.3	-1.3
H3		-0.1	-0.1	-0.1
		1.4	1.4	1.4
	-1.6	-0.6	-0.6	-0.6
N5	-1.5	-0.4	-0.4	-0.3
	50.7	50.3	50.8	50.6
	-13.8	-13.0	-12.7	-12.9
H6	-12.1	-11.7	-11.4	-11.6
	-5.2	-5.0	-4.7	-4.8
		-4.5	-4.5	-4.5
$H7_1$		-4.3	-4.3	-4.3
		-2.7	-2.7	-2.7
		-4.6	-4.6	-4.4
$H7_2$		-4.4	-4.3	-4.1
		-2.8	-2.7	-2.5
		-4.6	-4.5	-4.6
$H7_3$		-4.3	-4.2	-4.3
		-2.7	-2.6	-2.7

nuclei	AtC[3] (MHz)	AtC (MHz)	ErC (MHz)	ErD (MHz)
	11.7	11.7	11.0	11.2
$H8_1$	11.7	11.7	11.0	11.2
	14.0	13.9	13.2	13.4
	11.7	10.6	10.9	11.2
$H8_2$	11.7	10.7	10.9	11.2
	14.0	12.8	13.0	13.4
	11.7	11.2	11.4	11.3
$H8_3$	11.7	11.2	11.4	11.4
	14.0	13.4	13.6	13.5
		1.1	0.9	0.9
H9		2.4	2.2	2.3
		5.1	4.9	5.0
	0.1	0.2	0.1	0.2
N10	0.5	0.5	0.4	0.5
	18.9	17.9	17.8	17.9
	4.8	3.1	3.3	3.4
$H\beta_1$	5.2	3.4	3.7	3.8
	9.0	7.2	7.5	7.6
	2.0	2.3	2.3	2.2
$H\beta_2$	2.5	2.7	2.6	2.5
	6.4	6.2	6.2	6.0

3.4 Comparison of hyperfine coupling parameters in tryptophan

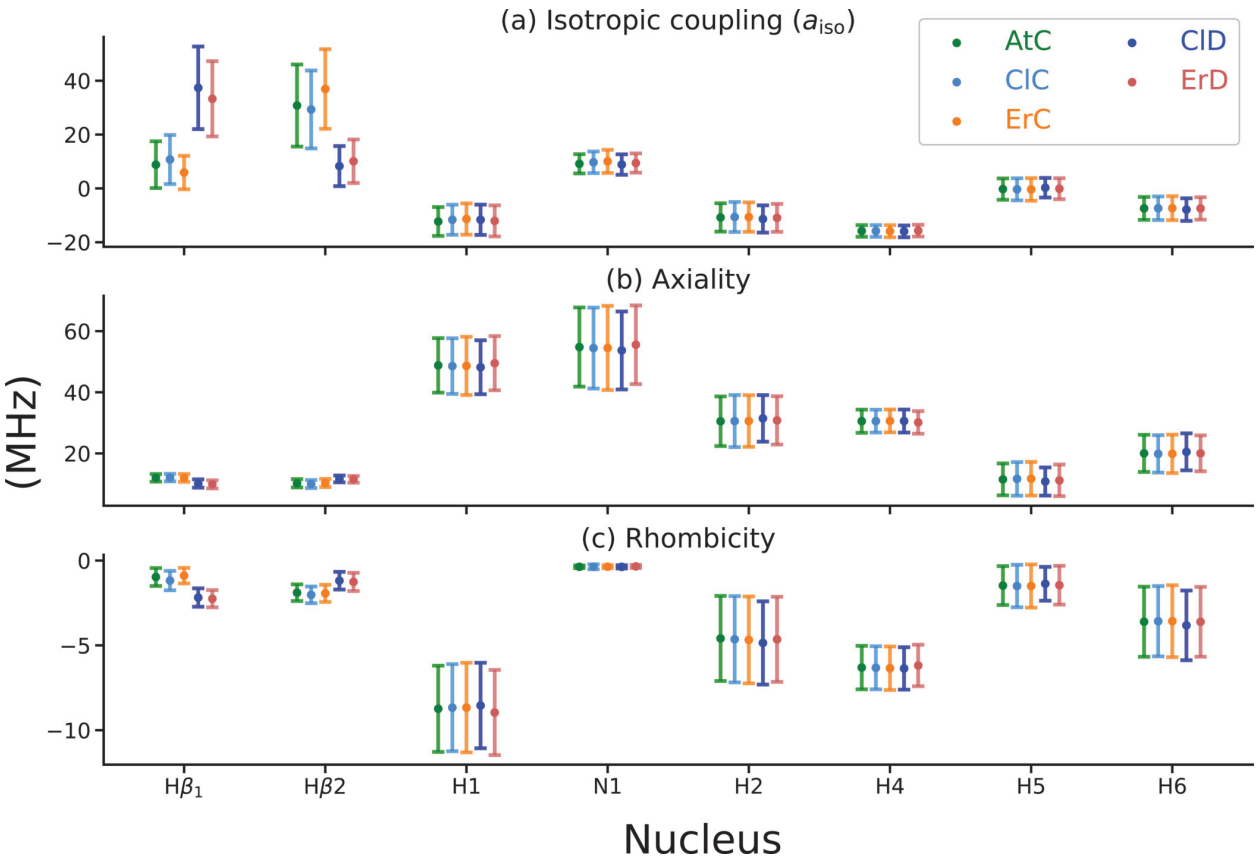

Figure S15: Comparison of the (a) isotropic value a_{iso}, (b) axiality and (c) rhombicity of the hyperfine coupling tensors of selected tryptophan nuclei in the five radical pairs, represented by error bars centred at the mean value with whiskers extending to one standard deviation on either side. Panel (a) is another representation of the isotropic coupling distribution data shown in Fig. S11 and Fig. S13.

A comparison of the hyperfine coupling parameters in the tryptophan radical for the five radical pairs is summarized in Fig. S15. Parameters plotted are (a) the isotropic coupling, (b) the axiality and (c) the rhombicity of each hyperfine tensor, obtained from the three principal values of the tensor (denoted as e_1, e_2 and e_3 with $e_1 < e_2 < e_3$) as follows:

$$\text{Isotropic coupling, } a_{\text{iso}} = \frac{1}{3}(e_1 + e_2 + e_3), \tag{S7}$$

$$\text{Axiality} = 2e_3 - (e_1 + e_2), \tag{S8}$$

$$\text{Rhombicity} = e_1 - e_2. \tag{S9}$$

3.5 Hyperfine coupling surface plots

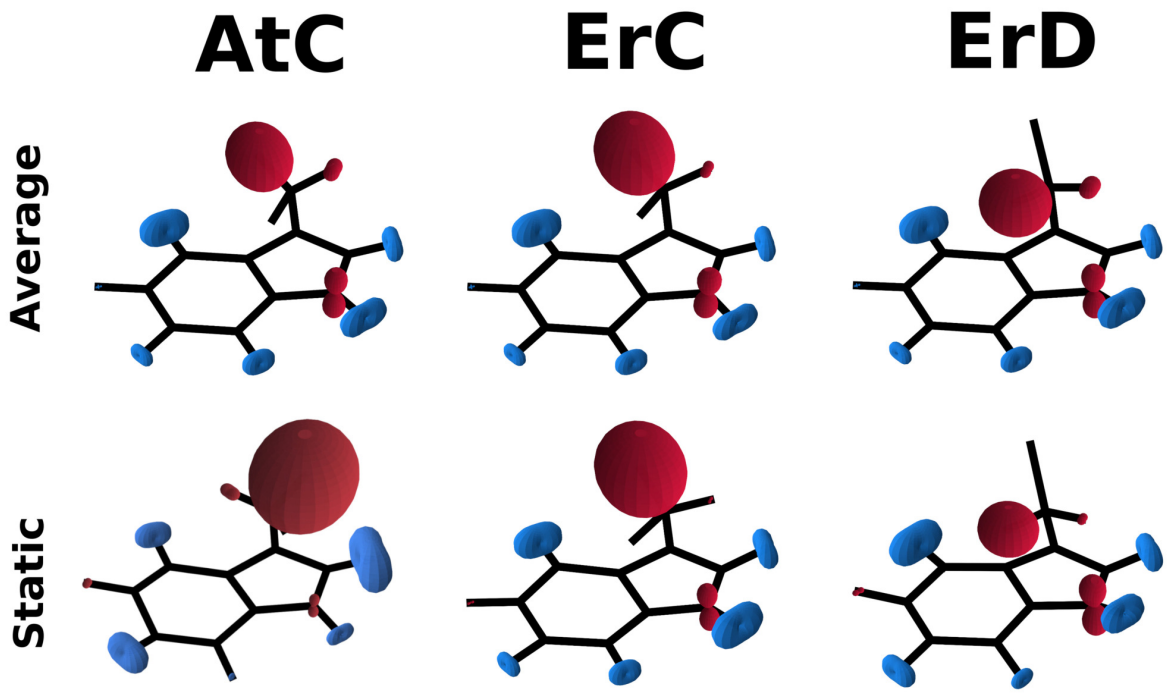

Figure S16: Three-dimensional surface plot representations of the full hyperfine tensors in $Trp^{\bullet+}$ averaged over 1200 ns (top row) and static hyperfine tensors obtained from the crystal structure of AtCry1 and for the equilibrated structures of ErC and ErD, i.e. for the first frame of the MD simulation of the respective RP (lower row). Only interactions of the magnetic H- and N-nuclei are displayed. Red (blue) lobes indicate a positive (negative) value of the trace of the hyperfine tensor with a larger lobe signifying a stronger hyperfine coupling and a more spherical lobe indicating a more isotropic hyperfine coupling tensor.

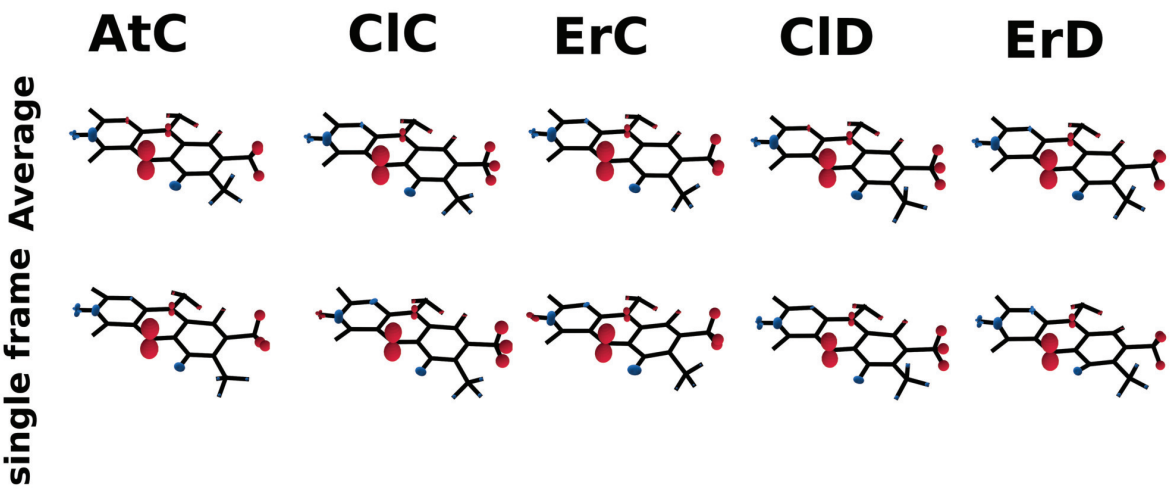

Figure S17: Three-dimensional surface plot representations of the full hyperfine tensors in $FAD^{\bullet-}$ averaged over 1200 ns (top row) and static hyperfine tensors obtained from the crystal structure of AtCry1 and for the equilibrated structures of ClC, ErC, ClD and ErD, i.e. for the first frame of the MD simulation of the respective RP (lower row). Only interactions of the magnetic H- and N-nuclei are displayed with the interactions of the N1, N3 and H3 nuclei scaled by a factor of 10 for better visibility. Red (blue) lobes indicate a positive (negative) value of the trace of the hyperfine tensor. The hyperfine tensors were plotted on the average coordinates of the $FAD^{\bullet-}$ extracted from the MD simulation of the respective RP system. An exception was made for the coordinates of the methyl atoms $H8_x$ and $H7_x$, whose relative positions to their methyl carbons were taken from the first frame of the MD simulation. There is almost no difference in the strength of the hyperfine coupling in the $FAD^{\bullet-}$ radicals from the different RP systems and the hyperfine coupling in the single MD frame and the average hyperfine coupling.

4 Compass sensitivity

4.1 Quantum yield calculation

```
// -------------------------------------------------------------
SpinSystem RPSystem
{
        // -----------------------------------------------------
        // Spins
        // -----------------------------------------------------
        Spin RPElectron1
        {
                type = electron;
                tensor = isotropic(2);
                spin = 1/2;
        }

        Spin RPElectron2
        {
                type = electron;
                tensor = isotropic(2);
                spin = 1/2;
        }
        Spin FN5
        {
                tensor = matrix("-1.2875e-05 -2.5054e-06 -5.0497e-05;-2.5054e-06 -2.1464e-05 1.1530e-05;-5.0497e-05 1.1530
    e-05 0.0018");
                spin = 1;
        }
        Spin FN10
        {
                tensor = matrix("1.4602e-05 -1.4315e-06 -5.9250e-06;-1.4315e-06 4.3469e-06 -7.9713e-06;-5.9250e-06 -7.9713
    e-06 0.0006");
                spin = 1;
        }
        Spin FH81
        {
                tensor = matrix("0.0004 0.0 0.0;0.0 0.0004 0.0;0.0 0.0 0.0004");
                spin = 1/2;
        }
        Spin FH82
        {
                tensor = matrix("0.0004 0.0 0.0;0.0 0.0004 0.0;0.0 0.0 0.0004");
                spin = 1/2;
        }
        Spin FH83
        {
                tensor = matrix("0.0004 0.0 0.0;0.0 0.0004 0.0;0.0 0.0 0.0004");
                spin = 1/2;
        }
        Spin WHB1
        {
                tensor = matrix("0.0003 -2.63015e-05 3.9318e-05;-2.6301e-05 0.0001 9.3906e-06;3.9318e-05 9.3906e-06 0.0002
    ");
                spin = 1/2;
        }
        Spin WHB2
        {
                tensor = matrix("0.0013 8.2499e-06 6.3855e-05;8.2499e-06 0.0012 5.3365e-05;6.3855e-05 5.3365e-05 0.0014");
                spin = 1/2;
        }
        Spin WNE1
        {
                tensor = matrix("7.6295e-05 0.0001 -8.8812e-05;0.0001 0.0006 -0.0004;-8.8812e-05 -0.0004 0.0004");
                spin = 1;
        }
        Spin WHE1
        {
                tensor = matrix("-0.0006 0.0002 0.0003;0.0002 -0.0004 0.0002;0.0003 0.0002 -0.0002");
                spin = 1/2;
        }
        Spin WHE3
        {
                tensor = matrix("-0.0006 0.0002 0.0002;0.0002 -0.0006 7.3025e-05;0.0002 7.3025e-05 -0.0005");
                spin = 1/2;
        }

        // -----------------------------------------------------
        // Interactions
        // -----------------------------------------------------
        Interaction zeeman1
        {
                type = zeeman;
                field = "4.357787137e-06 0 4.98097349e-05";
                spins = RPElectron1,RPElectron2;
        }

        Interaction radical1hyperfine
        {
                type = hyperfine;
                group1 = RPElectron1;
                group2 = FN5,FN10,FH81,FH82,FH83;
        }
        Interaction radical2hyperfine
        {
                type = hyperfine;
                group1 = RPElectron2;
                group2 = WHB1,WHB2,WNE1,WHE1,WHE3;
        }

        // -----------------------------------------------------
```

```
        // Spin States
        // ------------------------------------------------------------
        State Singlet   // |S>
        {
                spins(RPElectron1,RPElectron2) = |1/2,-1/2> - |-1/2,1/2>;
        }

        State T0        // |T0>
        {
                spins(RPElectron1,RPElectron2) = |1/2,-1/2> + |-1/2,1/2>;
        }

        State Tp        // |T+>
        {
                spin(RPElectron2) = |1/2>;
                spin(RPElectron1) = |1/2>;
        }

        State Tm        // |T->
        {
                spin(RPElectron2) = |-1/2>;
                spin(RPElectron1) = |-1/2>;
        }

        State Identity  // Identity projection
        {
        }

        // ------------------------------------------------------------
        // Transitions
        // ------------------------------------------------------------
        Transition Product1
        {
                type = sink;
                source = Identity;      // spin-independent reaction
                rate = 0.001;

        }

        // ------------------------------------------------------------
        // SpinSystem Properties
        // ------------------------------------------------------------
        Properties properties
        {
                Initialstate = Singlet;
        }
}
Settings
{
        // ------------------------------------------------------------
        // General settings
        // ------------------------------------------------------------
        Settings general
        {
                steps = 72;
        }

        // ------------------------------------------------------------
        // Actions
        // ------------------------------------------------------------
        Action scan
        {
                type = rotatevector;
                vector = RPSystem.zeeman1.field;
               axis = "0 0 1";
                value = 5.0;
        }

        // ------------------------------------------------------------
        // Outputs objects
        // ------------------------------------------------------------
        Output orientation
        {
                type = vectorxyz;
                vector = RPSystem.zeeman1.field;
        }
}
Run
{
        Task main
        {
               type = RP-SymmetricUncoupled;    // Specify task class
               logfile = "logfile.txt";
               datafile = "result.dat";
        }
}
```

Listing 3: Exemplary input file for the quantum singlet yield calculations using the open source software Molspin.[6] The code above calculates the singlet yield in ErC for a system with ten nuclear spins and an angle θ of five degrees of the magnetic field vector with the z-axis (Fig. 2). The azimuthal angle ϕ is varied in 72 steps by five degrees in each step. All time constants are given in nanoseconds and the hyperfine coupling is given in tesla in the reference frame defined using the central ring of the $FAD^{\bullet-}$.

4.2 Singlet yield anisotropy (including for the crystal structure of AtCry1)

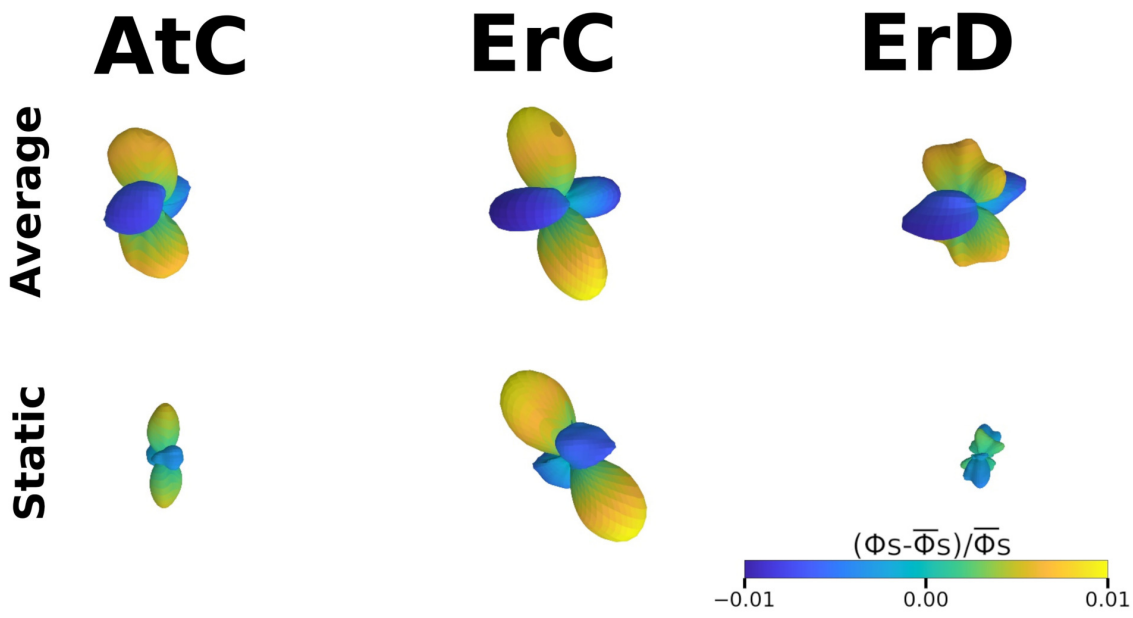

Figure S18: Anisotropy surface plots comparing the of calculation results based on the static and averaged hyperfine coupling tensors. The static hyperfine couplings for AtC are based on the crystal structure of AtCry1 while for ErC and ErD the hyperfine coupling tensors are taken for the structures after equilibration. The RPs in all calculations included the N5, N10, $H8_1$, $H8_2$ and $H8_3$ nuclei in $FAD^{\bullet-}$ and $H\beta_1$, $H\beta_2$, H1, N1 and H4 in $Trp^{\bullet+}$. The average of the hyperfine tensors was performed over 1200 ns of MD simulations.

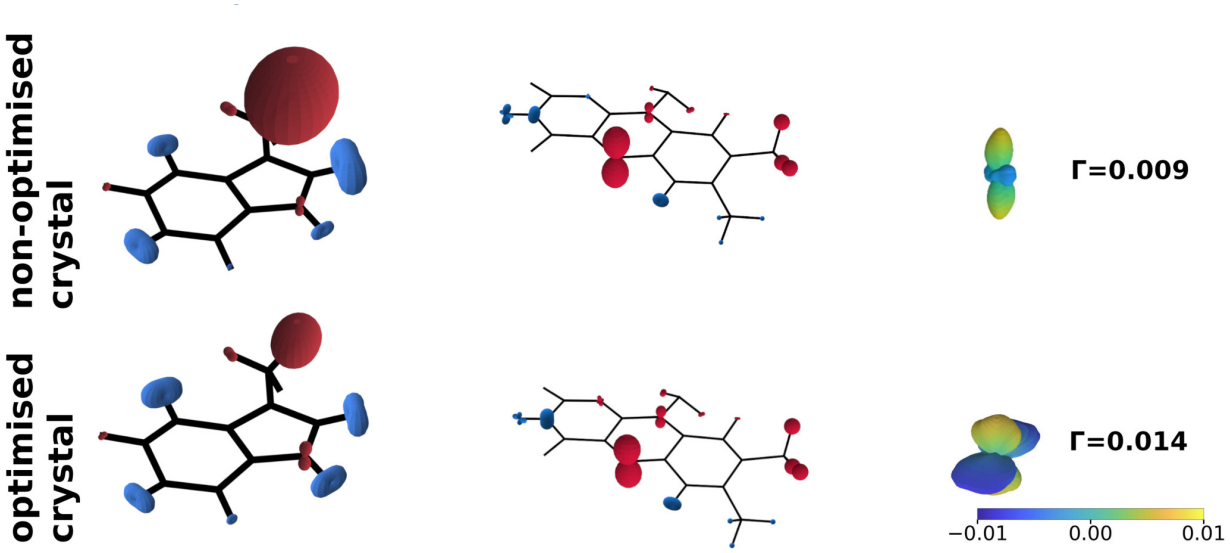

Figure S19: Comparison of the resulting hyperfine tensors in $Trp^{\bullet+}$ and $FAD^{\bullet-}$ and the anisotropy surface plots using the non-optimised (upper row) and optimised (lower row) crystal structure of AtCry1. Here, non-optimised signifies that only the positions of the hydrogen atoms used to terminate dangling bonds (circled in Fig. 2) were optimised. The input structures for the lower row were obtained by only freezing the dihedral angles Λ and Ω and optimising all other atom coordinates in dft calculations. Details about the representation of the hyperfine tensor surface plots and the anisotropy surface plots from Figs S16 - S18 apply.

4.3 Variation of Γ with the reaction rate constant

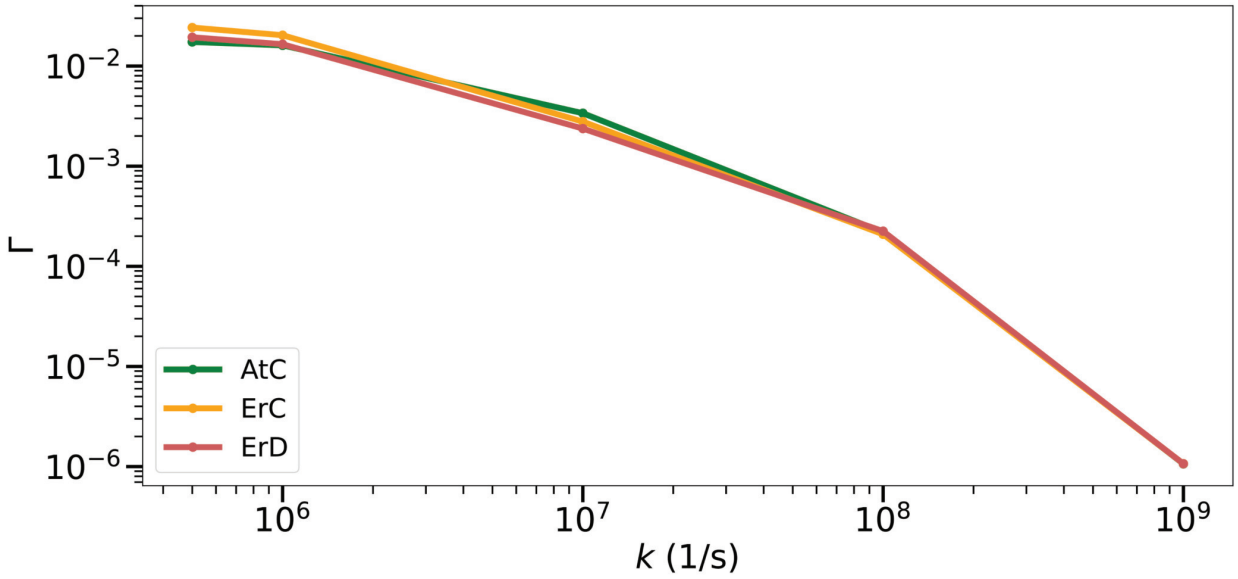

Figure S20: The singlet yield anisotropy Γ obtained for different values of the reaction rate constant $k_S = k_T = k$ (refer to Fig. 1 for the reaction scheme involving k_S and k_T). The RPs in all calculations included the N5, N10, $H8_1$, $H8_2$ and $H8_3$ nuclei in $FAD^{\bullet-}$ and $H\beta_1$, $H\beta_2$, H1, N1 and H4 in $Trp^{\bullet+}$.

4.4 Variation of Γ with the number of nuclei in the radical pair

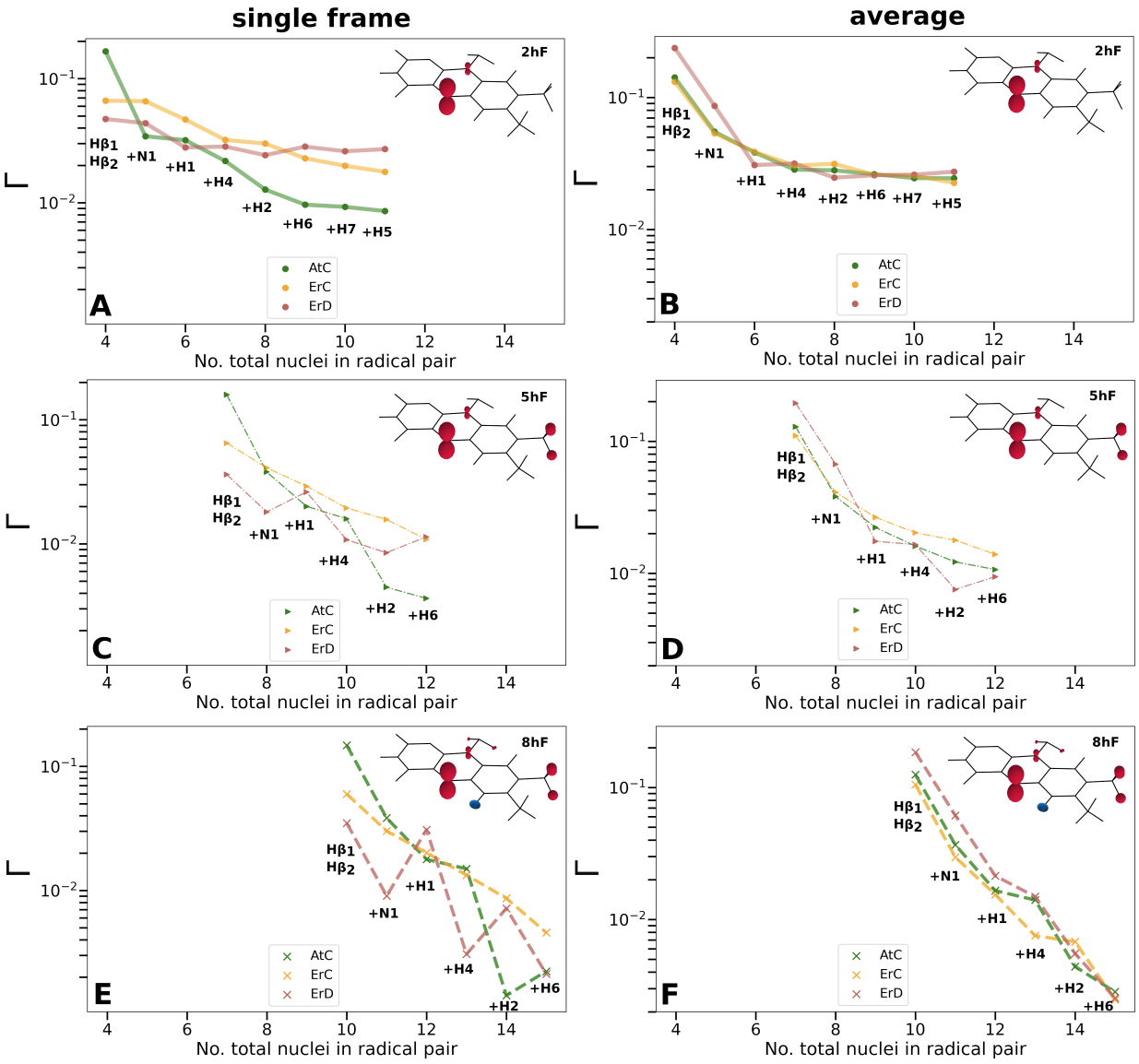

Figure S21: Singlet yield anisotropies calculated for RPs comprising different numbers of nuclei. The plots in the left column are based on hyperfine couplings calculated for a single frame from the MD simulations and the plots on the right are based on the MD-averaged hyperfine coupling over 1,200 ns. Each row contains RPs with the same number of hyperfine couplings in $FAD^{\bullet-}$, as illustrated in the upper right corner (labeled in Fig. 2). **A, B**: Hyperfine interactions of N5 and N10 in $FAD^{\bullet-}$ (**2hF**) are considered. **C, D**: N5, N10, $H8_1$, $H8_2$ and $H8_3$ (**5hF**). **E, F**: N5, N10, $H8_1$, $H8_2$, $H8_3$, H6, $H\beta_1$ and $H\beta_2$ (**8hF**). For the hyperfine interactions from nuclei in $Trp^{\bullet+}$, each RP simulation series was started with $H\beta_1$ and $H\beta_2$ and then N1, H1, H4, H2, H6, H7 and H5 were added one at a time in the order indicated by the labels in each plot.

4.5 Table of Γ values

Table S3: The singlet yield anisotropy Γ computed for the three RP systems with the averaged hyperfine interactions from the listed nuclei included in the spin Hamiltonian.

nuclei in $FAD^{\bullet-}$	nuclei in $Trp^{\bullet+}$	AtC	ErC	ErD
N5, N10	Hβ_1, Hβ_2	0.142	0.132	0.237
N5, N10	Hβ_1, Hβ_2,N1	0.055	0.054	0.086
N5, N10	Hβ_1, Hβ_2,N1,H1	0.038	0.039	0.031
N5, N10	Hβ_1, Hβ_2, N1, H1, H4	0.028	0.031	0.032
N5, N10	Hβ_1, Hβ_2 N1, H1, H4, H2	0.013	0.031	0.025
N5, N10	Hβ_1, Hβ_2 N1, H1, H4, H2, H6	0.010	0.026	0.026
N5, N10	Hβ_1, Hβ_2 N1, H1, H4, H2, H6, H7	0.025	0.026	0.026
N5, N10	Hβ_1, Hβ_2 N1, H1, H4, H2, H6, H7, H5	0.024	0.023	0.027
N5, N10, H8_1, H8_2, H8_3	Hβ_1, Hβ_2	0.129	0.110	0.195
N5, N10, H8_1, H8_2, H8_3	Hβ_1, Hβ_2, N1	0.038	0.041	0.067
N5, N10, H8_1, H8_2, H8_3	Hβ_1, Hβ_2, N1, H1	0.022	0.027	0.018
N5, N10, H8_1, H8_2, H8_3	Hβ_1, Hβ_2 N1, H1, H4	0.016	0.020	0.017
N5, N10, H8_1, H8_2, H8_3	Hβ_1, Hβ_2, N1, H1, H4, H2	0.012	0.018	0.008
N5, N10, H8_1, H8_2, H8_3	Hβ_1, Hβ_2, N1, H1, H4, H2, H6	0.011	0.014	0.009
N5, N10, H6, Hβ_1, Hβ_2, H8_1, H8_2, H8_3	Hβ_1, Hβ_2	0.125	0.105	0.185
N5, N10, H6, Hβ_1, Hβ_2, H8_1, H8_2, H8_3	Hβ_1, Hβ_2, N1	0.037	0.030	0.061
N5, N10, H6, Hβ_1, Hβ_2, H8_1, H8_2, H8_3	Hβ_1, Hβ_2, N1, H1	0.017	0.015	0.021
N5, N10, H6, Hβ_1, Hβ_2, H8_1, H8_2, H8_3	Hβ_1, Hβ_2 N1, H1, H4	0.014	0.008	0.015
N5, N10, H6, Hβ_1, Hβ_2, H8_1, H8_2, H8_3	Hβ_1, Hβ_2 N1, H1, H4, H2	0.004	0.007	0.006
N5, N10, H6, Hβ_1, Hβ_2, H8_1, H8_2, H8_3	Hβ_1, Hβ_2 N1, H1, H4, H2, H6	0.003	0.002	0.003

References

(1) Papoulis, A.; Pillai, S. U. *Probability, random variables, and stochastic processes*, 4th ed.; McGraw Hill: Boston, 2002; pp 90,190–191.

(2) Humphrey, W.; Dalke, A.; Schulten, K. VMD - Visual Molecular Dynamics. *J. Mol. Graph. Model.* **1996**, *14*, 33–38.

(3) Kattnig, D. R.; Solov'yov, I. A.; Hore, P. J. Electron spin relaxation in cryptochrome-based magnetoreception. *Phys. Chem. Chem. Phys.* **2016**, *18*, 12443–12456.

(4) Euklid, *Die Elemente*, 2nd ed.; Wissenschaftliche Buchgesellschaft: Darmstadt, 1962; Vol. 3; pp 67–68.

(5) Frisch, M. J. et al. Gaussian09 Revision D.01. **2013**, Gaussian Inc. Wallingford CT 2009.

(6) Nielsen, C.; Solov'yov, I. A. MolSpin—Flexible and extensible general spin dynamics software. *J. Chem. Phys.* **2019**, *151*, 194105.